bioRxiv preprint doi: https://doi.org/10.1101/484410; this version posted April 8, 2019. The copyright holder for this preprint (which was not certified by peer review) is the author/funder, who has granted bioRxiv a license to display the preprint in perpetuity. It is made available under aCC-BY-NC-ND 4.0 International license.

Precocious neuronal differentiation and disrupted oxygen responses in Kabuki syndrome

Giovanni A. Carosso[1,2], Leandros Boukas[1,2,3], Jonathan J. Augustin[2,4,5], Ha Nam Nguyen[6], Briana L. Winer[2], Gabrielle H. Cannon[2], Johanna D. Robertson[2], Li Zhang[2], Kasper D. Hansen[2,3], Loyal A. Goff[2,5], Hans T. Bjornsson[2,7,8,9]*

[1]Predoctoral Training Program in Human Genetics, McKusick-Nathans Institute of Genetic Medicine, Johns Hopkins University School of Medicine, Baltimore, United States.
[2]McKusick-Nathans Institute of Genetic Medicine, Johns Hopkins University School of Medicine, Baltimore, United States.
[3]Department of Biostatistics, Johns Hopkins University School of Medicine, Baltimore, United States.
[4]Predoctoral Training Program in Biochemistry, Cellular, and Molecular Biology, Johns Hopkins University School of Medicine, Baltimore, United States.
[5]Solomon H. Snyder Department of Neuroscience, Johns Hopkins University School of Medicine, Baltimore, United States.
[6]Institute for Cell Engineering, Johns Hopkins University School of Medicine, Baltimore, United States.
[7]Department of Pediatrics, Johns Hopkins University School of Medicine, Baltimore, United States.
[8]Faculty of Medicine, School of Health Sciences, University of Iceland, Reykjavik, Iceland.
[9]Landspitali University Hospital, Reykjavik, Iceland.
*Correspondence: hbjorns1@jhmi.edu

Abstract

Chromatin modifiers act to coordinate gene expression changes critical to neuronal differentiation from neural progenitor cells (NPCs). *KMT2D* encodes a histone methyltransferase that promotes transcriptional activation, and is frequently mutated in cancers and in the majority (>70%) of patients diagnosed with the congenital, multisystem intellectual disability (ID) disorder Kabuki syndrome 1 (KS1). While critical roles for KMT2D are established in various non-neuronal tissues, the effects of KMT2D loss in brain cell development have not been described. We conducted parallel studies of proliferation, differentiation, transcription, and chromatin profiling in KMT2D-deficient human and mouse models to define KMT2D-dependent functions in neurodevelopmental contexts, including adult-born hippocampal neural stem cells (NSCs) and NPCs *in vivo*. We report cell-autonomous defects in proliferation, cell cycle, and cell survival, accompanied by NSC depletion and precocious differentiation of NPCs *in vitro and in vivo*. Transcriptional suppression in KMT2D-deficient cells indicated perturbation of hypoxia-responsive cellular metabolism pathways, and functional experiments confirmed abnormalities of neuronal hypoxia response in cells with inactivated KMT2D. Together, our findings support a model in which loss of KMT2D function suppresses expression of oxygen-responsive gene programs in developing neural progenitors, resulting in precocious neuronal differentiation and exhaustion of the adult-born hippocampal progenitor pool.

bioRxiv preprint doi: https://doi.org/10.1101/484410; this version posted April 8, 2019. The copyright holder for this preprint (which was not certified by peer review) is the author/funder, who has granted bioRxiv a license to display the preprint in perpetuity. It is made available under aCC-BY-NC-ND 4.0 International license.

Introduction

Trithorax group proteins promote chromatin accessibility by exerting antagonistic functions against Polycomb group transcriptional suppressors to activate gene expression (1). Fine-tuning of cell type transitions during neuronal development depends critically on this duality, as evidenced by severe neurodevelopmental defects caused by variants in numerous chromatin-modifying genes (2). Loss-of-function variants in genes encoding two such enzymes, lysine-specific methyltransferase 2D (KMT2D) and X-linked lysine-specific demethylase 6A (KDM6A/UTX) cause the intellectual disability (ID) disorder Kabuki syndrome (KS1 and KS2, respectively) (3, 4). Up to 74% (5) of KS cases result from mutations in *KMT2D* (KS1), encoding a major histone H3 lysine 4 (H3K4) methyltransferase which catalyzes the placement of chromatin-opening modifications promoting gene expression at context-specific targets. Developmental requirements of KMT2D in cardiac precursors (6), B cells (7, 8), muscle and adipose (9), and epithelial tissues (10) have been linked, respectively, to *KMT2D*-associated cardiac, immunologic, and oncogenic contexts (11), yet the effects of KMT2D deficiency in neurodevelopment are not yet understood.

We previously described a mouse model of Kabuki syndrome, $Kmt2d^{+/\beta geo}$, demonstrating characteristic features of KS1 patients including postnatal growth retardation, craniofacial abnormalities, and visuospatial memory impairments, associating with decreased adult hippocampal neurogenesis in the dentate gyrus (DG) (12). Decreased grey matter volume in the human DG was subsequently observed in KS1 patients, further implicating this region in KS1-associated ID phenotypes (13). The continual birth and integration of new neurons makes adult neurogenesis the most potent form of lifelong plasticity in the mammalian brain (14), and has now been established in humans (15). During late embryonic stages, a subset of multipotent progenitors persists in the DG (16), becoming subject to an array of intrinsic and extrinsic factors affecting NSC maintenance, i.e. self-renewal, proliferation, and differentiation into NPCs and neurons, throughout adult life. Mounting evidence tightly links metabolic rewiring (17) and hypoxic states in the DG (18) to regulation of NSC maintenance and NPC differentiation, and understanding the role of KMT2D in these processes will be critical to development of postnatal interventions in KS1-associated ID. Furthermore, robust cellular models of neurodevelopmental disruption in KS1 are needed to appreciate the target gene- and cell type-specific impact of KMT2D loss on brain function. Such studies have the potential to identify primary molecular consequences of KMT2D loss and facilitate targeted disease-modifying therapeutic approaches.

Here, we first report that KMT2D loss disrupts proliferation, cell cycle, and cell survival in a manner consistent across mouse and human KS1 neurodevelopment models. We then compare

bioRxiv preprint doi: https://doi.org/10.1101/484410; this version posted April 8, 2019. The copyright holder for this preprint (which was not certified by peer review) is the author/funder, who has granted bioRxiv a license to display the preprint in perpetuity. It is made available under aCC-BY-NC-ND 4.0 International license.

transcriptional and KMT2D binding profiles to prioritize KS1-associated target genes in mouse hippocampal cells specifically lacking KMT2D catalytic activity, identifying disruption of HIF1-regulated, oxygen-responsive cellular metabolism pathways, prompting functional experiments which demonstrated KMT2D-dependent neuronal responses to hypoxia. To assess translational potential of our results in humans, we generated KS1 patient-derived iPSC and NPC models, confirming proliferation, cell cycle, and cell survival defects, before using single-cell transcriptome analysis to probe gene expression perturbances along the NPC development trajectory. Surprisingly, we observed hallmarks of precocious neuronal maturation in differentiating KS1 NPCs. Finally, we explore relevancy of these findings *in vivo*, identifying depletion of adult-born hippocampal NSCs, accompanied by cell cycle defect, global transcriptional suppression, and precocious NPC differentiation in *Kmt2d*-deficient adult mice.

bioRxiv preprint doi: https://doi.org/10.1101/484410; this version posted April 8, 2019. The copyright holder for this preprint (which was not certified by peer review) is the author/funder, who has granted bioRxiv a license to display the preprint in perpetuity. It is made available under aCC-BY-NC-ND 4.0 International license.

Results

Genetic ablation of the *Kmt2d* SET methyltransferase domain disrupts cell proliferation and cell cycle in a cell-autonomous manner

We selected the HT22 mouse hippocampal neuronal cell line (19) for detailed analysis of KMT2D function in neuronal context. We generated distinct *Kmt2d*-inactivating alleles (biological replicates on an isogenic background) and analyzed each one in both heterozygosity and homozygosity, enabling gene dosage-dependent studies. Specifically, gDNA sequence encoding the SET methyltransferase domain was deleted by CRISPR-Cas9 with an upstream small guide RNA (sgRNA^{up}) in exon 52 and either sgRNA^{1} (exon 54) or sgRNA^{2} (intron 54), resulting in deletions of 565 (*Kmt2d*$^{\Delta1}$) or 654 bp (*Kmt2d*$^{\Delta2}$), respectively (**Supplementary Figure 1A**). Mutations were characterized to base-pair resolution by Sanger DNA sequencing and *in silico* translation to predict protein products (**Supplementary Figure 1A'**). Targeted cells were identified by PCR (**Supplementary Figure 1B**) and clonally expanded to establish heterozygous (*Kmt2d*$^{+/\Delta}$) and homozygous (*Kmt2d*$^{\Delta/\Delta}$) cell lines for comparison against the parental wild-type line (*Kmt2d*$^{+/+}$). *Kmt2d* mRNA was analyzed by RT-qPCR demonstrating ~50% decreased message of the targeted region in *Kmt2d*$^{+/\Delta}$ cells and no message in *Kmt2d*$^{\Delta/\Delta}$ cells (**Supplementary Figure 1C**), and confirmed specificity of the deletion, leaving intact mRNA message of exons upstream of the deletion site. Immunofluorescence using a KMT2D antibody, with antigenicity upstream of our mutations, confirmed presence of KMT2D protein in all genotypes, demonstrating distinctly nuclear distribution in *Kmt2d*$^{+/+}$ cells but more diffuse distribution in *Kmt2d*$^{+/\Delta}$ and *Kmt2d*$^{\Delta/\Delta}$ cells, as well as uniformly nuclear expression of neuronal nuclei marker RBFOX3/NeuN (**Figure 1A**).

Proliferation analysis, performed 72 hours after equal-density plating, revealed cell densities ~52% lower in *Kmt2d*$^{+/\Delta}$ cells and ~39% lower in *Kmt2d*$^{\Delta/\Delta}$ cells, compared to wild-type (**Figure 1B**). Proliferation defects were supported independently by CellTrace Violet generational tracking, detecting less dilution of a fluorescent tracer, i.e. fewer cell divisions, in *Kmt2d*$^{\Delta/\Delta}$ daughter cells compared to wild-type over 72 hours (**Figure 1C**, left, **Supplementary Figure 1D**). As control, genotype had no effect on parental cell uptake of the fluorescent tracer (**Figure 1C**, right). Flow cytometric analysis of cell cycle occupancy at steady-state, using marker of proliferation Ki-67 (KI67) and a DNA label, revealed that *Kmt2d*$^{+/\Delta}$ cells and *Kmt2d*$^{\Delta/\Delta}$ cells were enriched for S and G_2 phase, compared to wild-type (**Figure 1D, Supplementary Figure 1E-E'**). To characterize temporal dynamics of cell cycle progression, we synchronized cells in G_2/M phase using nocodazole, and analyzed DNA content at timepoints after release (**Figure 1E**). We observed wild-type cells exiting G_2/M phase at

bioRxiv preprint doi: https://doi.org/10.1101/484410; this version posted April 8, 2019. The copyright holder for this preprint (which was not certified by peer review) is the author/funder, who has granted bioRxiv a license to display the preprint in perpetuity. It is made available under aCC-BY-NC-ND 4.0 International license.

significantly higher rates than *Kmt2d*$^{\Delta/\Delta}$ cells, beginning at 3 hours and up to 18 hours after release (**Figure 1E'**). Finally, cell death was profiled by flow cytometric detection of caspase-3/7 substrate cleavage and SYTOX uptake, distinguishing early apoptotic and necrotic cells. Apoptotic, but not necrotic, cell proportions were greater in both *Kmt2d*$^{+/\Delta}$ cells (~287%) and *Kmt2d*$^{\Delta/\Delta}$ cells (~478%) compared to wild-type (**Figure 1F**).

Findings of proliferative defects, G_2/M cell cycle delay, and increased apoptosis in *Kmt2d*-inactivated hippocampal cells, upon selective targeting of the SET catalytic domain, support a cell-autonomous role for KMT2D activity and make this an attractive model for detailed transcriptional and chromatin profiling of KMT2D function in a neuronal context.

bioRxiv preprint doi: https://doi.org/10.1101/484410; this version posted April 8, 2019. The copyright holder for this preprint (which was not certified by peer review) is the author/funder, who has granted bioRxiv a license to display the preprint in perpetuity. It is made available under aCC-BY-NC-ND 4.0 International license.

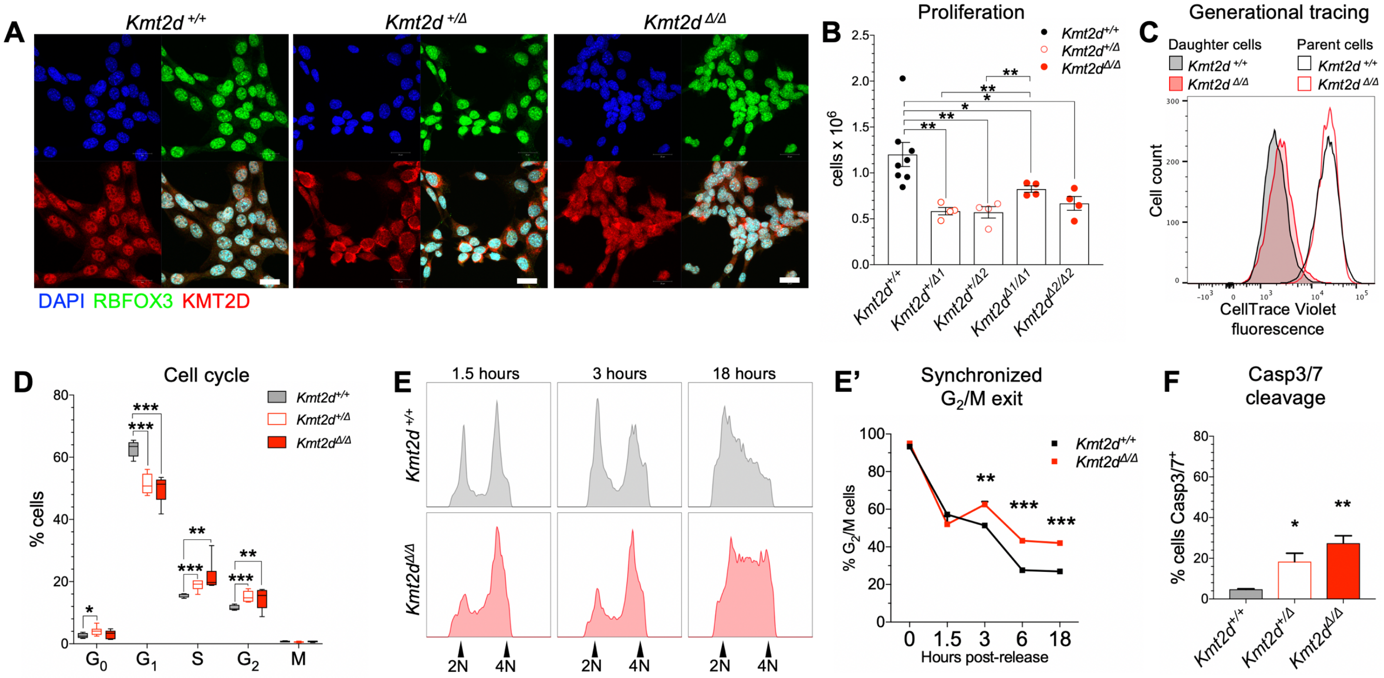

Figure 1. Genetic ablation of the *Kmt2d* SET methyltransferase domain disrupts cell proliferation and cell cycle in a cell-autonomous manner. (**A**) Representative immunostaining against KMT2D and neuronal nuclei marker RBFOX3 in HT22 mouse hippocampal cells, including wild-type (*Kmt2d*$^{+/+}$) and KMT2D-inactivated cells (*Kmt2d*$^{+/\Delta}$ and *Kmt2d*$^{\Delta/\Delta}$). (**B**) Decreased proliferation in *Kmt2d*-inactivated cells quantified 72 hours after equal density plating (7 wells per cell line). (**C**) Generational tracking by CellTrace Violet dye in *Kmt2d*$^{+/+}$ and *Kmt2d*$^{\Delta/\Delta}$ cells over 72 hours. Higher mean fluorescence intensity indicates less dye dilution, i.e. fewer cell divisions, in *Kmt2d*$^{\Delta/\Delta}$ daughter cells (left) at 72 hours. Negative control, parental cells confirm equal, genotype-independent uptake of CellTrace (right) at 0 hours. (**D**) Flow cytometric quantification of cell cycle at steady-state in HT22 cells (5 wells per cell line) by gating on KI67 and DAPI fluorescence (DNA content). (**E**) *Kmt2d*$^{+/+}$ and *Kmt2d*$^{\Delta/\Delta}$ cells synchronized in G_2/M and released for time course analysis of G_2/M exit, by DNA content, up to 18 hours after release, and (**E'**) quantification of cells in G_2/M (technical triplicates per time point). (**F**) Flow cytometric quantification of early apoptotic cells using fluorescence coupled to caspase-3/7 peptide cleavage in *Kmt2d*$^{+/+}$, *Kmt2d*$^{+/\Delta}$, and *Kmt2d*$^{\Delta/\Delta}$ cells (3-6 wells per cell line). Bars indicate mean±SEM. Asterisks indicate significance from control mean, Student's t-test (*$p<0.05$, **$p<0.01$, ***$p<0.001$).

bioRxiv preprint doi: https://doi.org/10.1101/484410; this version posted April 8, 2019. The copyright holder for this preprint (which was not certified by peer review) is the author/funder, who has granted bioRxiv a license to display the preprint in perpetuity. It is made available under aCC-BY-NC-ND 4.0 International license.

Suppressed transcription of KMT2D- and HIF-regulated hypoxia response genes upon loss of the KMT2D SET methyltransferase domain

We performed high-coverage RNA-seq comparing three *Kmt2d*$^{\Delta/\Delta}$ clones against the parental *Kmt2d*$^{+/+}$ line, each in technical triplicate, followed by differential expression analysis. Libraries robustly clustered by genotype, with clear separation of *Kmt2d*$^{\Delta/\Delta}$ cells from *Kmt2d*$^{+/+}$ by Principal Component Analysis (PCA) of gene expression, yielding 575 significant differentially-expressed genes (DEGs) at a False Discovery Rate (FDR) of 0.05 in *Kmt2d*$^{\Delta/\Delta}$ cells compared to *Kmt2d*$^{+/+}$ (**Figure 2A-A',** (**Supplementary Figure 2A-B**, **Supplementary Table 1**). ~76% of significant DEGs (436 genes) were downregulated (down hereafter) in *Kmt2d*$^{\Delta/\Delta}$ cells, consistent with strong global suppression of gene expression upon *Kmt2d* inactivation, including known KMT2D target genes such as Krueppel-like factor 10 (*Klf10*) (12). Overrepresentation analysis (ORA) determined several significantly enriched gene networks among *Kmt2d*$^{\Delta/\Delta}$ down DEGs, including glycolysis, hypoxia-inducible factor 1 (HIF1) signaling, RAS signaling, autophagy, and others, while *Kmt2d*$^{\Delta/\Delta}$ upregulated DEGs (up hereafter) were enriched in fewer networks (**Figure 2B**).

KMT2D-mediated transcriptional activation occurs in a target gene-specific manner, so we reasoned that among the 575 observed *Kmt2d*$^{\Delta/\Delta}$ DEGs, a subset of genes found to also bind KMT2D itself, in wild-type cells, would more likely represent direct transcriptional consequences of *Kmt2d* inactivation, whereas non-bound DEGs could reflect indirect effects. We performed chromatin immunoprecipitation followed by high-throughput sequencing (ChIP-seq) with a previously validated ChIP-grade KMT2D antibody (9) in *Kmt2d*$^{+/+}$ HT22 cells. This identified 3,756 KMT2D binding peaks significantly enriched over input (**Supplementary Table 2**), of which ~10% occur inside promoters and ~33% (1,235 peaks) occur within 5 kb of a gene transcription start site (TSS±5kb, **Supplementary Figure 2C-E**). To account for promoter and enhancer interactions (9, 10, 20), we reasoned that TSS±5kb peaks more likely constitute a cis-regulatory function of KMT2D binding on proximal genes, and we will refer to these as KMT2D-bound genes. The 1,463 KMT2D-bound genes in neuronal cells (**Supplementary Table 3**) were significantly enriched in mRNA 3'UTR binding, rho GTPase signaling, circadian clock, translation elongation, oxidative stress-induced senescence, HIF1 signaling, and other pathways (**Supplementary Figure 2F**).

We then intersected KMT2D-bound genes with *Kmt2d*$^{\Delta/\Delta}$ DEGs to reveal 74 putative direct target genes (**Table 1**), of which ~85% (63 genes) were as expected downregulated (**Figure 2C**), including insulin-like growth factor 1 (*Igf1*), fos-like antigen 2 (*Fosl2*). At least 20 observed KMT2D-bound, *Kmt2d*$^{\Delta/\Delta}$ DEGs were previously described as KMT2D targets in other tissues (7, 21),

bioRxiv preprint doi: https://doi.org/10.1101/484410; this version posted April 8, 2019. The copyright holder for this preprint (which was not certified by peer review) is the author/funder, who has granted bioRxiv a license to display the preprint in perpetuity. It is made available under aCC-BY-NC-ND 4.0 International license.

suggesting some KMT2D target conservation across cell types. KMT2D-bound, *Kmt2d*$^{\Delta/\Delta}$ down-DEGs were most significantly enriched for face morphogenesis, glycolytic process, protein kinase B signaling, hypoxia response, and cell proliferation pathways (**Figure 2C'**), and surprisingly, 29 of these 63 genes are known to be HIF1-regulated (22). KMT2D-ChIP peaks on HIF1-regulated genes clustered at promoters and enhancers, often overlapping CpG islands in genes such as *Fosl2*, with others clustering at alternative TSSs, as in retinoic acid receptor alpha (*Rara*), or in enhancer-like peaks as in DNA-damage-inducible transcript 4 (*Ddit4*) (**Figure 2D**, **Supplementary Figure 2G-G'**).

A significant fraction of KMT2D-bound, *Kmt2d*$^{\Delta/\Delta}$ DEGs control oxygen-responsive metabolism, warranting interrogation of KMT2D and HIF1A binding site overlaps which could implicate a cis-regulatory role for KMT2D in cellular oxygen responses. We first intersected our significant KMT2D-ChIP peak sequences with regions previously determined HIF1A-bound in embryonic heart (23), yielding 423 regions overlapping with base pair resolution (**Figure 2E**). Like KMT2D, HIF1A showed ~10% of peaks located inside promoters, but among overlapping KMT2D/HIF1A-bound peaks this fraction approached ~40%, supporting cooperative cis-regulatory activity by these factors (**Figure 2E', Supplementary Figure 2E**). Remarkably, we observed 289 TSS±5kb genes, as defined above, for these overlapped KMT2D/HIF1A-bound peaks, 8 of which are *Kmt2d*$^{\Delta/\Delta}$ DEGs: *Ddit4*, heat shock protein family D member 1 (*Hspd1*), Cbp/p300-interacting transactivator with Glu/Asp-rich C-terminal domain 2 (*Cited2*), DAZ associated protein 1 (*Dazap1*), WASH complex subunit 4 (*Washc4*), transducer of (*Errb2*), 1 (*Tob1*), carboxypeptidase Q (*Cpq*), leucine rich pentatricopeptide repeat containing 4 (*Lrpprc*).

To determine if KMT2D/HIF1A-regulated genes generalize to additional tissues, and restricting analysis to promoters, we next interrogated independent sets of genes with experimentally validated, hypoxia-induced HIF1A binding at the promoter (24). Of 86 validated genes, 5 were KMT2D-bound, *Kmt2d*$^{\Delta/\Delta}$ down-DEGs in neuronal cells, a 23.3-fold greater frequency than that expected by chance (odds ratio 23.3, p=4.74e-6): *Ddit4*, *Cited2*, aldolase A (*Aldoa*), Bcl2/adenovirus E1B 19-KD protein-interacting protein 3-like (*Bnip3l*), and ceruloplasmin (*Cp*). Of 81 genes validated in three or more distinct tissues, 3 were KMT2D-bound, *Kmt2d*$^{\Delta/\Delta}$ down-DEGs in neuronal cells (odds ratio=14.03, p=0.002): *Klf10*, *Rara*, and *Ddit4*. Of note, these genes are known to have important roles regulating cellular differentiation in addition to mediating oxygen responses.

Given the significant occurrence of *Kmt2d*$^{\Delta/\Delta}$ down-DEGs for oxygen response in neuronal cells at normoxic culture conditions, including shared and direct KMT2D/HIF1A targets, we hypothesized that KMT2D may be required for transcriptional response to changes in cellular oxygen pressure. To test this in a *Kmt2d* dosage-dependent manner, we subjected *Kmt2d*$^{+/+}$ cells, *Kmt2d*$^{+/\Delta}$ cells, and

bioRxiv preprint doi: https://doi.org/10.1101/484410; this version posted April 8, 2019. The copyright holder for this preprint (which was not certified by peer review) is the author/funder, who has granted bioRxiv a license to display the preprint in perpetuity. It is made available under aCC-BY-NC-ND 4.0 International license.

Kmt2d$^{\Delta/\Delta}$ cells to normoxic (20% O_2) or hypoxic (1% O_2) conditions, then analyzed hypoxia-induced gene expression. RT-qPCR analysis of the canonical HIF1A targets vascular endothelial growth factor A (*Vegfa*), Bcl2/adenovirus E1B 19-KD protein-interacting protein 3 (*Bnip3*), DNA-damage-inducible transcript 3 (*Ddit3*), and cyclin-dependent kinase inhibitor 1A (*Cdkn1A*) revealed the expected gene induction, up to several-fold, upon hypoxic exposure over baseline in *Kmt2d*$^{+/+}$ cells; in contrast, *Kmt2d*$^{+/\Delta}$ and *Kmt2d*$^{\Delta/\Delta}$ cell lines failed to induce expression of hypoxia-inducible genes to comparable levels (**Figure 2F**).

Upon cellular sensing of low oxygen, activated HIF1A becomes stabilized against cytoplasmic degradation and undergoes nuclear translocation, so we next quantified the proportion of cellular HIF1A fluorescence colocalizing in the nucleus, under normoxic and hypoxic conditions (**Supplementary Figure 2H**). Unexpectedly, under normoxic conditions *Kmt2d*$^{\Delta/\Delta}$ cells exhibited ~2-fold greater proportion of nuclear HIF1A (~17.5%) than *Kmt2d*$^{+/+}$ cells (~8.8%), and this difference increased further upon hypoxic exposure (**Supplementary Figure 2H'**). In *Kmt2d*$^{+/\Delta}$ cells, nuclear HIF1A fraction (~7.3%) was comparable to wild-types in normoxia, but in hypoxia sharply increased to ~24.8%. *Kmt2d*$^{+/+}$ cells in the same hypoxia paradigm showed modestly increased nuclear HIF1A, suggesting a lower threshold for hypoxic HIF1A translocation in *Kmt2d*$^{+/\Delta}$ cells and constitutive HIF1A translocation in *Kmt2d*$^{\Delta/\Delta}$ cells. We again observed over-representation in G_2/M phase occupancy in normoxia in *Kmt2d*$^{\Delta/\Delta}$ cells compared to *Kmt2d*$^{+/+}$ cells, and observed a mild increase of G_2/M phase occupancy in hypoxia for all genotypes (**Supplementary Figure 2H''**). Flow cytometric quantification of caspase-3/7 activity demonstrated sharp decreases in apoptotic cell fractions in all genotypes under hypoxia (**Supplementary Figure 2I-I'**). In contrast, necrotic cell fractions detected by SYTOX fluorescence were similar across genotypes in normoxia, but under hypoxia decreased only in *Kmt2d*$^{+/+}$ cells and *Kmt2d*$^{+/\Delta}$ cells, while marginally increasing in *Kmt2d*$^{\Delta/\Delta}$ cells (**Supplementary Figure 2I''**).

Taken together, data from *Kmt2d*-inactivated mouse neuronal cells suggest that KMT2D plays an important role in positive regulation of cellular proliferation and oxygen-responsive, HIF1-inducible gene expression, including direct targets important to cellular differentiation. The cell-autonomous nature of these *Kmt2d*-dependent phenotypes raises the question of whether such effects apply to human cells, and furthermore what, if any, consequences occur in the context of neuronal differentiation.

bioRxiv preprint doi: https://doi.org/10.1101/484410; this version posted April 8, 2019. The copyright holder for this preprint (which was not certified by peer review) is the author/funder, who has granted bioRxiv a license to display the preprint in perpetuity. It is made available under aCC-BY-NC-ND 4.0 International license.

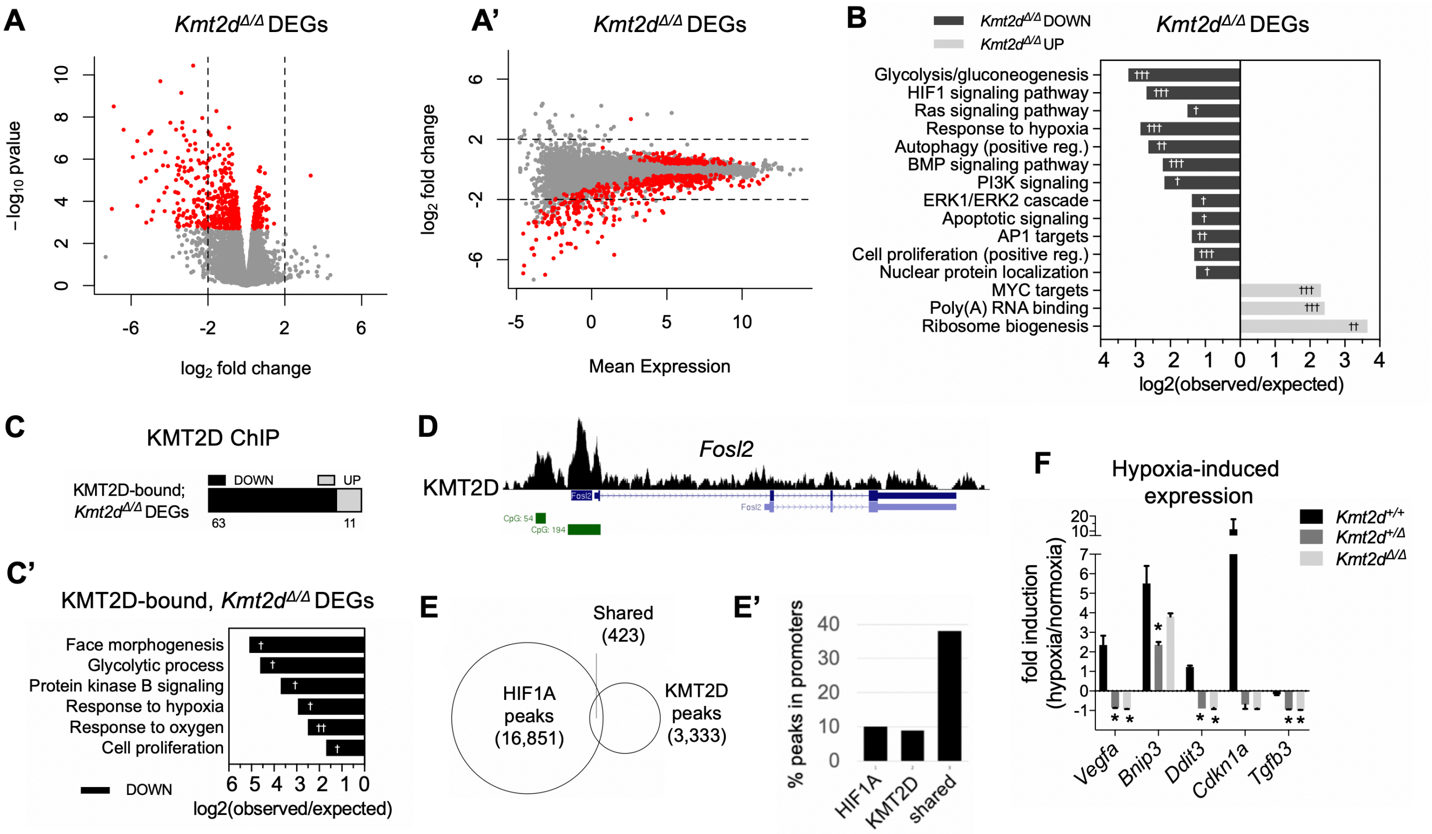

Figure 2. Suppressed transcription of KMT2D- and HIF-regulated hypoxia response genes upon loss of the *Kmt2d* SET methyltransferase domain in neuronal cells. (**A-A'**) Expression analysis by RNA-seq in HT22 mouse neuronal cells reveals 575 significant differentially expressed genes (DEGs) in *Kmt2d*$^{\Delta/\Delta}$ clones (3 biological replicates) relative to *Kmt2d*$^{+/+}$ cells, each in technical triplicate. Fold changes in expression indicate most significant *Kmt2d*$^{\Delta/\Delta}$ DEGs (~76%, red dots) are downregulated in *Kmt2d*$^{\Delta/\Delta}$ cells, plotted against (**A**) p-value and (**A'**) mean expression. (**B**) Gene networks significantly enriched among down- or up-regulated *Kmt2d*$^{\Delta/\Delta}$ DEGs. (**C**) *Kmt2d*$^{\Delta/\Delta}$ DEGs which are also KMT2D-bound, as determined by ChIP-seq chromatin profiling in *Kmt2d*$^{+/+}$ HT22 cells, and (**C'**) gene networks significantly enriched among KMT2D-bound, *Kmt2d*$^{\Delta/\Delta}$ DEGs. (**D**) Representative ChIP-seq track of a KMT2D-bound, *Kmt2d*$^{\Delta/\Delta}$ DEG depicting KMT2D binding peaks (black), RefSeq gene annotations (blue), and CpG islands (green). (**E**) Overlapping loci of observed KMT2D-ChIP peaks in HT22 cells and HIF1A-ChIP peaks in embryonic heart (23). (**E'**) Overlapping KMT2D/HIF1A peak regions, compared to individually bound regions, are enriched at gene promoters. (**F**) RT-qPCR analysis of hypoxia-induced gene expression in *Kmt2d*$^{+/+}$, *Kmt2d*$^{+/\Delta}$, and *Kmt2d*$^{\Delta/\Delta}$ cells, following 72 hours in normoxia (20% O_2) or hypoxia (1% O_2), with fold induction of HIF1A target gene mRNA (2 biological replicates per genotype, each in technical triplicate; negative fold changes plotted as negative reciprocal). Fisher's Exact Test (†FDR<0.05, ††FDR<0.01, †††FDR<0.001); *significance from wild-type induction, Student's t-test (*p<0.05, **p<0.01, ***p<0.001).

bioRxiv preprint doi: https://doi.org/10.1101/484410; this version posted April 8, 2019. The copyright holder for this preprint (which was not certified by peer review) is the author/funder, who has granted bioRxiv a license to display the preprint in perpetuity. It is made available under aCC-BY-NC-ND 4.0 International license.

KS1 patient-derived cells recapitulate KMT2D-associated defects in proliferation and cell cycle

We reprogrammed skin biopsy fibroblasts to generate induced pluripotent stem cells (iPSCs) from a female with molecularly confirmed KS1 bearing a heterozygous nonsense *KMT2D* mutation (c.7903C>T:p.R2635*), and characteristic KS1 features including growth retardation, classical facial features, and congenital heart disease. Neuropsychological testing in a previous longitudinal study (25) of this patient had revealed a visuospatial memory impairment similar to that described in retrospective and prospective studies of KS1 patients (12, 26). KS1 iPSCs (KS1-1) bearing normal 46, XX karyotype (**Supplementary Figure 3A**) and characteristic iPSC morphology (**Figure 3A**) were selected for comparison against two independently generated, previously described iPSC lines (C1-2, C3-1) from unrelated healthy controls (27). KS1 iPSCs were predicted to be *KMT2D* haploinsufficient due to nonsense-mediated decay (NMD), and RT-qPCR confirmed decreased *KMT2D* mRNA compared to controls, with equivalently decreased expression of exons upstream and downstream of the mutation site as expected for a nonsense mutation (**Supplementary Figure 3B-C**). Flow cytometric analyses following pulse of cell division marker 5-ethynyl-2′-deoxyuridine (EdU) demonstrated lower proliferation rates (~25%) in KS1 iPSCs compared to controls (**Figure 3B**), accompanied by a shift in cell cycle occupancy (**Figure 3C, Supplementary Figure 3D**) toward overrepresentation of G_2/M phase cells (24% higher in KS1) and underrepresentation of G_0/G_1 phase cells (23% lower in KS1).

We next generated nestin (NES)-expressing NPCs through parallel differentiation of KS1 and control iPSCs using an established small molecule inhibition protocol (28). RT-qPCR confirmed decreased *KMT2D* also in KS1 NPCs (**Supplementary Figure 3E**) and both KS1 and control NPCs displayed normal NPC morphology (**Figure 3D, Supplementary Figure 3F**). Immunostaining against histone marks in KS1 NPCs detected significantly reduced fluorescence of open chromatin mark H3K4me2 (~65%) and increased fluorescence of closed chromatin marks H3K27me3 (~99%) and H3K9me3 (~180%) compared to controls (**Supplementary Figure 3G-I**). Compared to iPSC data, KS1 NPCs relative to control showed a markedly greater reduction in dividing cells as detected by EdU incorporation (~47%, **Figure 3E**) as well as fewer mitotic divisions over a 72-hour period as detected by CellTrace Violet (**Supplementary Figure 3J**). Unlike in iPSCs, cell cycle abnormalities were not observed in KS1 NPCs (**Figure 3F, Supplementary Figure 3K**) suggesting this phenotype may be cell-type dependent or lost during induced differentiation. However, flow cytometric analysis revealed higher proportions of cell death in KS1 cells compared to controls among both iPSCs (~130%) and NPCs (~115%) (**Figure 3G, Supplementary Figure 3L**).

bioRxiv preprint doi: https://doi.org/10.1101/484410; this version posted April 8, 2019. The copyright holder for this preprint (which was not certified by peer review) is the author/funder, who has granted bioRxiv a license to display the preprint in perpetuity. It is made available under aCC-BY-NC-ND 4.0 International license.

Finally, to determine whether the cell cycle G_2/M bias in KS1 iPSCs occurs in additional KS1 patients and unmanipulated primary cells, we performed cell cycle analysis in primary fibroblasts from two additional molecularly confirmed KS1 patients (KS1-2, KS1-3) in addition to KS1-1 and two additional healthy controls. KS1 and control fibroblasts were treated with nocodazole to synchronize in G_2/M phase, and flow cytometric DNA content analysis at 0- and 3-hours post-release demonstrated exit from G_2/M phase among control fibroblasts, but this was markedly decreased in fibroblasts of KS1 patients (**Figure 3H-H'**). Thus, delayed exit from G_2/M was consistent in primary cells from three independent KS1 patients.

bioRxiv preprint doi: https://doi.org/10.1101/484410; this version posted April 8, 2019. The copyright holder for this preprint (which was not certified by peer review) is the author/funder, who has granted bioRxiv a license to display the preprint in perpetuity. It is made available under aCC-BY-NC-ND 4.0 International license.

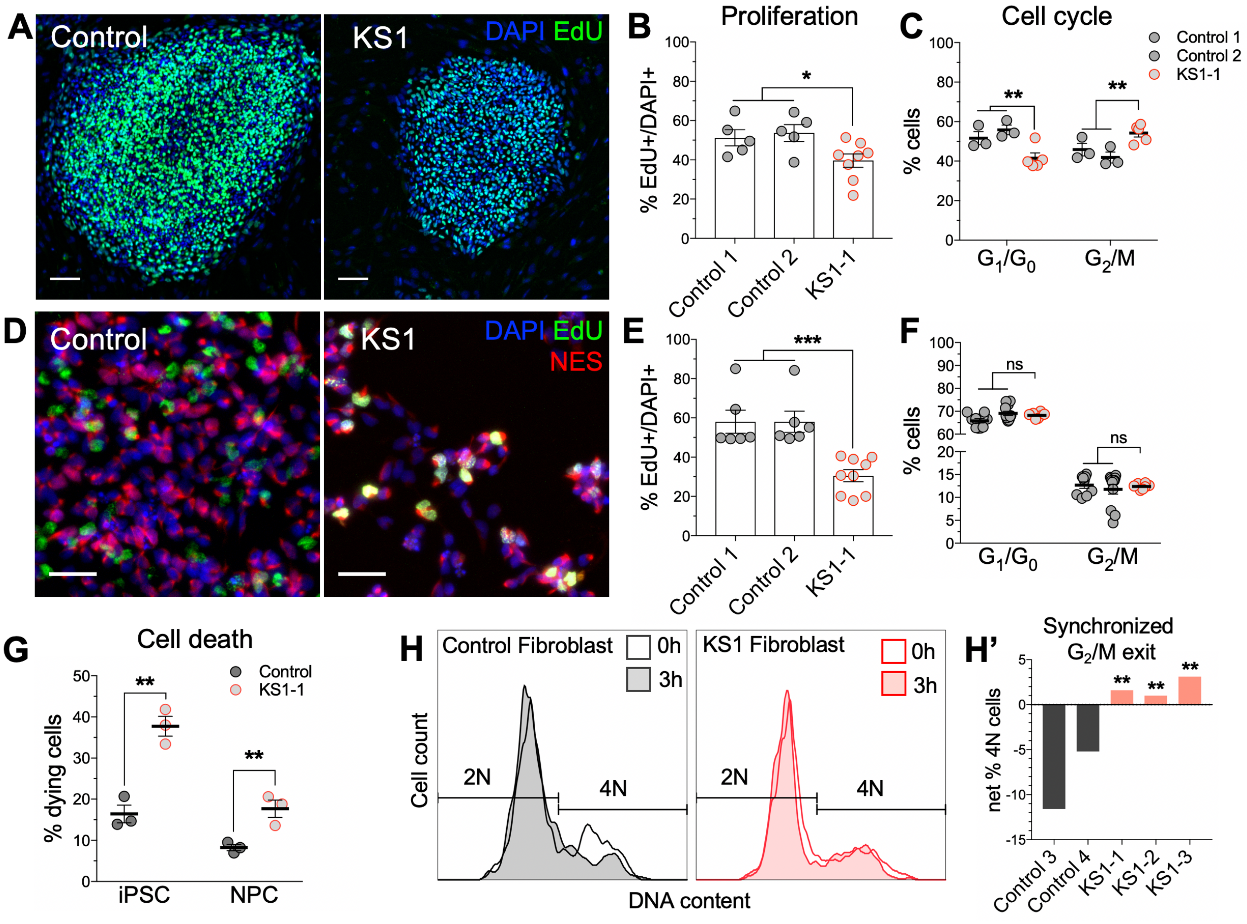

Figure 3. KS1 patient-derived cells recapitulate KMT2D-associated defects in proliferation and cell cycle. (**A**) Representative immunostaining of iPSCs from a confirmed *KMT2D*$^{+/-}$ KS1 patient (c.7903C>T:p.R2635*) and healthy controls, showing normal colony morphology. (**B**) Proliferative cells (5-8 wells per cell line) were pulsed with EdU for 30 minutes and quantified by flow cytometry. (**C**) Cell cycle analysis in iPSCs (3-5 wells per cell line), discriminating 2N and 4N DNA content (G_1/G_0 and G_2/M, respectively) by flow cytometry using DAPI fluorescence. (**D**) Representative immunostaining of NPCs induced from iPSCs of KS1 patient and controls, showing expected NPC morphology, nestin (NES) staining, and proliferative cells (EdU$^+$). (**E**) Proliferative cells (6-9 wells per cell line) were pulsed with EdU for 30 minutes and quantified by flow cytometry. (**F**) Cell cycle analysis in NPCs (8-12 wells per cell line), discriminating 2N and 4N DNA content (G_1/G_0 and G_2/M, respectively) by flow cytometry using DAPI fluorescence. (**G**) Quantification of dying cells by flow cytometric scatter profiles in iPSCs and NPCs (3 wells per cell line) from KS1 patient and controls. (**H-H'**) Synchronized G_2/M exit analysis by flow cytometry in fibroblasts from additional KS1 patients (KS1-1, KS1-2, KS1-3) and healthy controls (Controls 3 and 4), in triplicate per cell line. Cells were enriched for G_2/M phase using nocodazole and analyzed by DAPI fluorescence to and quantify (**H'**) G_2/M phase cell fractions at 0 and 3 hours after release. Bars indicate mean ± SEM. Asterisks indicate significance from control mean. Student's t-test (*p<0.05, **p<0.01, ***p<0.001).

bioRxiv preprint doi: https://doi.org/10.1101/484410; this version posted April 8, 2019. The copyright holder for this preprint (which was not certified by peer review) is the author/funder, who has granted bioRxiv a license to display the preprint in perpetuity. It is made available under aCC-BY-NC-ND 4.0 International license.

Transcriptional suppression of metabolic genes in cycling cells, and hallmarks of precocious neuronal differentiation in KS1 patient-derived NPCs

To interrogate transcriptional consequences of *KMT2D* loss in the context of neuronal differentiation, we performed single-cell RNA sequencing (scRNA-seq) in iPSCs and NPCs from the KS1 patient and controls (**Supplementary Figure 4A**). We first inspected cell clusters for expression of known iPSC or NPC markers to further verify cell identities, confirming that iPSCs displayed characteristic expression of pluripotency markers including POU domain, class 5, transcription factor 1 (*POU5F1*) (**Supplementary Figure 4B**), while NPCs expressed known markers of early neural lineage including paired box protein Pax-6 (*PAX6*) (**Supplementary Figure 4C**). A subset of NPCs further expressed neuronal maturation markers including microtubule-associated protein 2 (*MAP2*) (**Supplementary Figure 4D**).

First, differential expression analysis in iPSCs and NPCs identified genes downregulated or upregulated in KS1 patient relative to healthy controls (**Supplementary Figure 4E**). KS1 iPSCs displayed strong transcriptional suppression among 421 significantly differentially expressed genes (DEGs), with 372 genes (~88%) down and only 49 genes (~12%) up (**Supplementary Table 4**). In contrast, NPCs, following small molecule induction, showed less directional bias with 346 significant DEGs identified, among which 147 genes (~42%) were down and 199 genes (~58%) were up (**Supplementary Table 5**). We reasoned that despite differences in global expression trends between iPSCs and NPCs, genes shared down in both KS1 iPSCs and NPCs may be more likely to represent robust targets of KMT2D. Intersection of DEG lists showed that 40 genes were shared down in KS1 iPSCs and NPCs and 10 genes were shared up (**Supplementary Figure 4F-G, Supplementary Table 6**). Shared down genes included the glycolysis genes aldehyde dehydrogenase 7 family member A1 (*ALDH7A1*), enolase 1 (*ENO1*), and triosephosphate isomerase 1 (*TPI1*), as well as factors important to stem cell maintenance including proliferation-associated protein 2G4 (*PA2G4*) and protein lin-28 homolog A (*LIN28A*). Interestingly, some genes such as *TPI1* and *PA2G4* had also been observed down in *Kmt2d*-inactivated mouse neuronal cells (**Supplementary Table 1**). Similar to *Kmt2d*-deficient neuronal cells, downregulated genes in both patient-derived models were significantly enriched for HIF1A direct targets, genes containing the hypoxia-responsive element (HRE) 5'-RCGTG-3' motif, and known hypoxia response genes (**Supplementary Figure 4H**).

We next focused specifically on NPCs from KS1 patient and controls to better understand transcriptional abnormalities during neuronal differentiation. We used Uniform Manifold Approximation and Projection (UMAP) to visualize single cells in a manner that displays high-dimensionality data

bioRxiv preprint doi: https://doi.org/10.1101/484410; this version posted April 8, 2019. The copyright holder for this preprint (which was not certified by peer review) is the author/funder, who has granted bioRxiv a license to display the preprint in perpetuity. It is made available under aCC-BY-NC-ND 4.0 International license.

while preserving both local and global relationships (29). Cells of both control NPC lines were tightly clustered, indicating similar expression profiles, in contrast to a distinct separation of KS1 patient cells which appears to gradually lessen in a subset (top) of cells that more closely resemble controls (**Figure 4A**). We then used marker expression to partition single-cell libraries into developmentally informative subsets as follows. First, as control, we verified that differences in cell cycle phase composition do not account for KS1-associated differential gene expression in NPCs (**Supplemental Figure 5A-A'', Supplementary Table 7**). Next, we partitioned cells by expression of maturation stage-specific genes to defined an NPC differentiation trajectory consisting of early or "cycling" NPCs, "transitioning" NPCs, and "differentiating" NPCs (**Figure 4B**). We observed that cycling cells comprise the vast majority of NPCs analyzed and exhibit the greatest KS1-associated expression differences (**Figure 4B**, purple cells), while expression profiles of transitioning and differentiating NPCs show gradual convergence of gene expression (**Figure 4B**, grey and yellow cells, respectively). We analyzed DEGs exclusively within cycling, transitioning, and differentiating NPC subsets to determine if particular gene networks drive transcriptional differences in a stage-specific manner (**Figure 4C, Supplementary Table 7**). The most prevalent networks overall, NMD, translation initiation, and protein targeting, were strongly enriched regardless of maturation stage. In contrast, DEGs in transitioning NPCs, and to a lesser extent cycling NPCs, show enrichment of genes comprising the Notch signaling pathway including delta-like protein 3 (*DLL3*), protein jagged-1 (*JAG1*), transcription factor HES-5 (*HES5*), and cyclin D1 (*CCND1*). Cycling NPCs had DEGs enriched in glycolysis pathways including *ENO1*, *TPI1*, polyadenylate-binding protein 1 (*PABPC1*), L-lactate dehydrogenase L-chain (*LDHA*), *ALDOA,* and pyruvate kinase PKM (*PKM*), the latter two genes having also been observed as KMT2D-bound, *Kmt2d*$^{\Delta/\Delta}$ down genes in mouse neuronal cells.

Apart from increased rates of KS1 cell death (**Figure 3G**), another factor potentially contributing to the observed decrease of proliferative KS1 NPCs (**Figure 3E**) would be a change in cellular differentiation, such as precocious cell maturation, resulting in depletion of cycling precursors. To explore this in detail with scRNA-seq data, we examined expression of markers ranging from immature cells (*PAX6*$^{+}$) to the most differentiated cells (*MAP2*$^{+}$) (**Figure 4D-D'**). We further restricted analysis exclusively to the transitioning and differentiating, i.e. "maturing" NPC subset (**Supplementary Figure 5A'**), defining a trajectory that enabled parsing of cells into binned deciles of increasing maturation (**Supplementary Figure 5B-E''**). Quantification of cell densities revealed strong bias of KS1 NPCs in the most matured bins relative to controls (**Figure 4E**), i.e. greater representation of mature NPCs from KS1 than controls. These transcriptional signatures of precocious maturation

bioRxiv preprint doi: https://doi.org/10.1101/484410; this version posted April 8, 2019. The copyright holder for this preprint (which was not certified by peer review) is the author/funder, who has granted bioRxiv a license to display the preprint in perpetuity. It is made available under aCC-BY-NC-ND 4.0 International license.

were corroborated at protein level by flow cytometric analysis, finding KS1 NPCs had increased MAP2 fluorescence and reciprocally decreased PAX6 fluorescence relative to control (**Figure 4F-F'**).

Together, these results link transcriptional suppression of cellular metabolic pathways to cell-autonomous proliferation defects in *KMT2D*-deficient KS1 patient-derived stem cell models, revealing striking similarities to phenotypes and gene expression profiles in *Kmt2d*-deficient mouse neuronal cells. Furthermore, scRNA-seq data suggest that precocious differentiation may contribute to KS1-associated neurodevelopmental defects, however a stronger demonstration would be to observe these phenotypes *in vivo*, in an animal model established to phenocopy ID-related features of KS1 patients such as visuospatial memory impairments.

bioRxiv preprint doi: https://doi.org/10.1101/484410; this version posted April 8, 2019. The copyright holder for this preprint (which was not certified by peer review) is the author/funder, who has granted bioRxiv a license to display the preprint in perpetuity. It is made available under aCC-BY-NC-ND 4.0 International license.

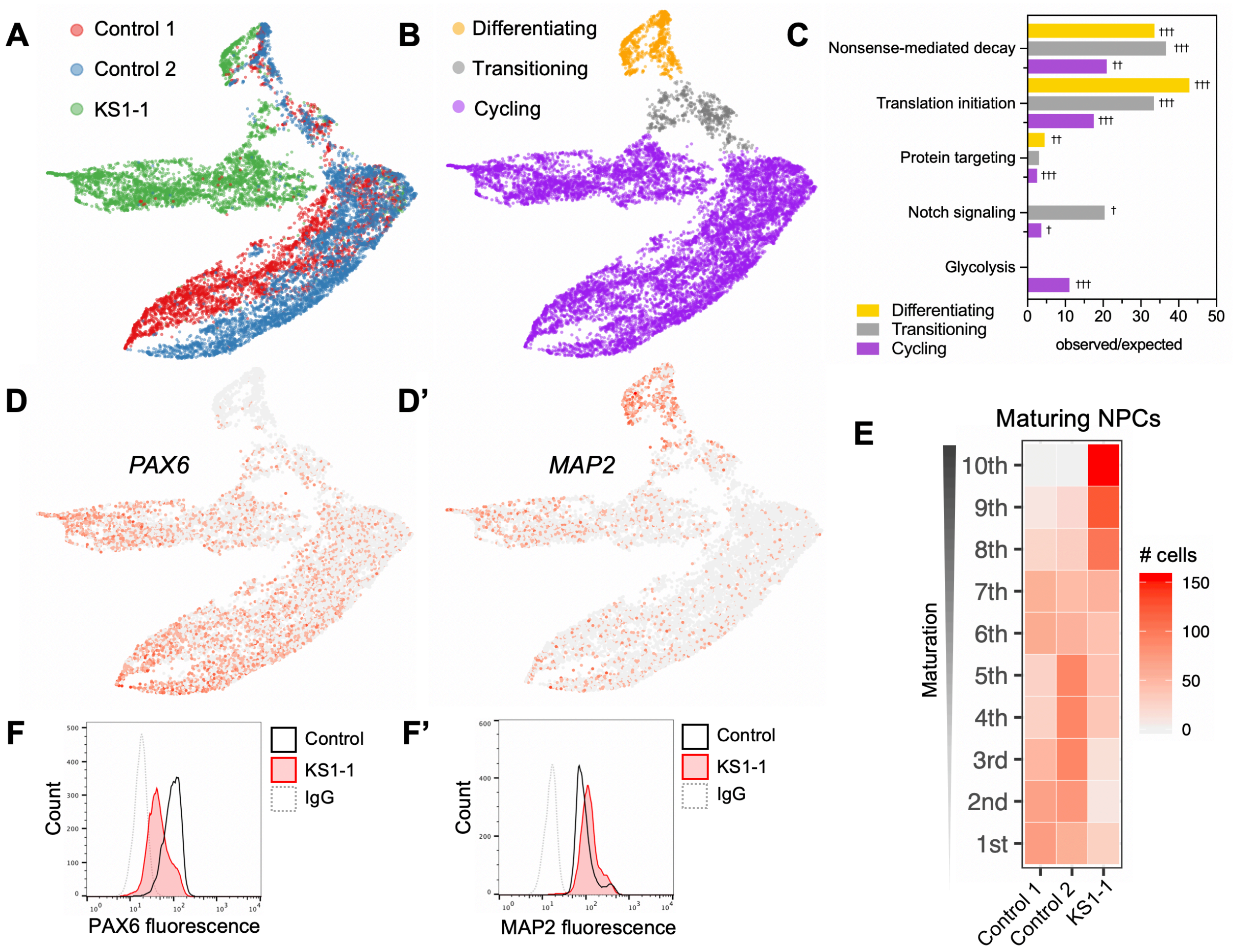

Figure 4. Transcriptional suppression of metabolic genes in cycling cells, and hallmarks of precocious neuronal differentiation in KS1 patient-derived NPCs. (**A**) Single-cell RNA-seq profiling in patient and healthy control iPSC-derived NPCs (~5,000 cells per patient), with Uniform Manifold Approximation Projection (UMAP) to visualize gene expression differences between cells. (**B**) NPCs partitioned by NPC maturation stage as defined by stage-specific marker expression, and (**C**) enriched gene networks, analyzed exclusively among DEGs for each NPC subset (cycling, transitioning, and differentiating). (**D-D'**) UMAPs annotated by relative expression intensities of NPC markers revealing the maturation trajectory from (**D**) early NPC (*PAX6*$^{+}$) to (**D'**) differentiating NPC (*MAP2*$^{+}$). (**E**) Heatmap comparing density of maturing NPCs along the maturation trajectory, defined by binned marker expression from earliest (1st) to most differentiated (10th) deciles, with KS1 cells disproportionately occupying the most mature bins. (**F-F'**) Flow cytometric validation of protein marker expression in NPCs from KS1 patient and controls, plotting fluorescence intensities of (**F**) early NPC marker PAX6 and (**F'**) mature NPC marker MAP2. (Fisher's Exact Test, †FDR<0.05, ††FDR<0.01, †††FDR<0.001).

bioRxiv preprint doi: https://doi.org/10.1101/484410; this version posted April 8, 2019. The copyright holder for this preprint (which was not certified by peer review) is the author/funder, who has granted bioRxiv a license to display the preprint in perpetuity. It is made available under aCC-BY-NC-ND 4.0 International license.

In vivo NSC depletion and precocious NPC differentiation in a *Kmt2d*$^{+/\beta geo}$ mouse model of Kabuki syndrome

Finally, we asked whether proliferative defects, transcriptional suppression, and precocious differentiation phenotypes observed *in vitro* using mouse neuronal cells and KS1 patient-derived stem cell models generalize to *in vivo* studies in an established KS1 mouse model. *Kmt2d*$^{+/\beta geo}$ mice, bearing a heterozygous *Kmt2d* SET domain mutation, were previously found to exhibit visuospatial memory impairments and reductions of doublecortin (DCX^{+}) and pulsed EdU^{+} cells in the DG (12, 30), but detailed analysis of neurogenic lineage progression and cycling NPC phenotypes in *Kmt2d*$^{+/\beta geo}$ mice has not been performed.

For cell cycle and RNA-seq analysis in *Kmt2d*$^{+/\beta geo}$ mice, we employed an EdU pulse paradigm to label dividing cells in 8-week old mice, and sampled micro-dissected DG within 1 cell cycle (16 hours) in order to capture the full complement of adult-born, dividing NPCs (**Figure 5A-A'**), then purifying EdU^{+} nuclei by fluorescence-activated cell sorting (FACS) (**Figure 5B**, **Supplementary Figure 6A**). Analysis of DNA content in the EdU^{+} population revealed enrichment in G_2/M phase and paucity of G_0/G_1 phase (**Figure 5C**), as observed in KMT2D-deficient *in vitro* models. We next performed transcriptional profiling by RNA-seq in purified EdU^{+} DG nuclei, yielding 827 DEGs (**Supplementary Figure 6B**, **Supplementary Table 8**). Among 416 down genes in *Kmt2d*$^{+/\beta geo}$ nuclei, the most significant enrichments were for misfolded protein binding, TCA cycle, proteasome complex, oxygen response, and poly(A) RNA-binding genes (**Supplementary Figure 6C**). Among genes upregulated we observed the upstream pro-apoptosis gene caspase-8 (*Casp8*) in these *Kmt2d*$^{+/\beta geo}$ proliferative nuclei. Given the observed downregulation of poly(A) RNA-binding genes, we considered the possibility that improper 3'UTR-mediated mRNA metabolism could lead to accumulation of transcripts influencing NPC maturation. Indeed, despite little overall bias in up- or downregulation among *Kmt2d*$^{+/\beta geo}$ proliferative nuclei, interrogation of canonical positive regulators of neuronal differentiation revealed a marked predominance of pro-neural transcripts upregulated, having only 3 genes down but 14 genes up, including copine-1 (*Cpne1*), focal adhesion kinase 1 (*Ptk2*), ras-related protein RAB11A (*Rab11A*), and retinoblastoma-associated protein 1 (*Rb1*). Interestingly, KS1 patient NPCs had also shown upregulated pro-neural genes such as nuclear receptor subfamily 2, group F, member 1 (*NR2F1*), pro-neural transcription factor HES-1 (*HES1*), and the GABAergic interneuron-promoting ladybird homeobox 1 (*LBX1*), and *Kmt2d*$^{\Delta/\Delta}$ mouse neuronal cells *in vitro* compared to wild-type had significantly higher mRNA levels of brain-derived neurotrophic factor (*Bdnf*) and neuron-specific microtubule element (*Tubb3/Tuj1*). Such pro-neural gene expression observed across KS1 models raises the possibility that NPC differentiation states could be altered in *Kmt2d*$^{+/\beta geo}$ mice.

bioRxiv preprint doi: https://doi.org/10.1101/484410; this version posted April 8, 2019. The copyright holder for this preprint (which was not certified by peer review) is the author/funder, who has granted bioRxiv a license to display the preprint in perpetuity. It is made available under aCC-BY-NC-ND 4.0 International license.

To examine NPC lineage progression *in vivo*, we compared stage-specific cell abundances both at steady-state and after pulse-label birth dating of adult-born NPCs. We used immunostaining markers (**Supplementary Figure 6D**) to compare abundance of individual DG cell precursor stages of adult mice 8 weeks old, comparing *Kmt2d*$^{+/\beta geo}$ mice to sex- and age-matched *Kmt2d*$^{+/+}$ littermates (**Figure 5D-D'**).

At steady-state, overall we observed significantly fewer neural progenitors in *Kmt2d*$^{+/\beta geo}$ mice compared to *Kmt2d*$^{+/+}$ mice at all stages analyzed, indicating that heterozygous *Kmt2d* loss impacts multiple NPC stages in the adult DG (**Figure 5D''**). Importantly, quiescent radial glia-like (qRGL, NES$^+$/MCM2$^-$) NSCs were ~39% less numerous in *Kmt2d*$^{+/\beta geo}$ mice compared to *Kmt2d*$^{+/+}$ mice, indicating a baseline depletion of the adult hippocampal NSC pool. Activated RGL (aRGL, NES$^+$/MCM2$^+$) NSCs were ~43% less numerous compared to *Kmt2d*$^{+/+}$ littermates, and intermediate progenitor cells (IPCs) (NES$^-$/MCM2$^+$), were ~26% fewer. We confirmed our prior observations (12, 30) of reduced representation at the neuroblast, or immature neuron, stage (DCX$^+$) of NPCs, finding a 28% decrease in *Kmt2d*$^{+/\beta geo}$ mice compared to *Kmt2d*$^{+/+}$ littermates. By stratifying our analysis anatomically along the septotemporal axis of the DG, we observe that aRGL NSC reductions in *Kmt2d*$^{+/\beta geo}$ mice were more pronounced in the septal DG than the temporal region (**Supplementary Figure 6E-E'**), congruous with *in vivo* spatial memory defects previously observed (12) which have been localized to this specific DG region (31). Because DCX$^+$ NPCs characteristically migrate radially during differentiation, we compared radial distances of DCX$^+$ cell bodies from the SGZ plane and observed increased distances in *Kmt2d*$^{+/\beta geo}$ mice compared to *Kmt2d*$^{+/+}$ littermates (**Supplementary Figure 6F**). Finally, despite reductions of NPC populations in *Kmt2d*$^{+/\beta geo}$ mice, we observed no numeric differences among mature neurons in the DG (RBFOX3/NeuN$^+$, **Supplementary Figure 6G**), nor were any gross abnormalities uncovered with post-mortem MRI volumetric analysis (**Supplementary Figure 6H, Supplementary Table 9**).

From these data, we then calculated a lineage progression index to approximate the expansion potential of each successive neurogenic cell type. Although *Kmt2d*$^{+/\beta geo}$ mice showed fewer total cells of each type at steady-state, the lineage progression index at each cell-type transition did not differ significantly in *Kmt2d*$^{+/\beta geo}$ mice, in fact appearing modestly higher in early-stage transitions in *Kmt2d*$^{+/\beta geo}$ mice, suggesting that particular cell-type transition impairments are not responsible for the adult neurogenesis defect in *Kmt2d*$^{+/\beta geo}$ mice (**Supplementary Figure 6I**). We did note a substantially higher coefficient of variation in *Kmt2d*$^{+/\beta geo}$ mice at the qRGL-to-aRGL progression stage, suggesting

bioRxiv preprint doi: https://doi.org/10.1101/484410; this version posted April 8, 2019. The copyright holder for this preprint (which was not certified by peer review) is the author/funder, who has granted bioRxiv a license to display the preprint in perpetuity. It is made available under aCC-BY-NC-ND 4.0 International license.

impaired coordination of NSC activation or increased stochasticity in mitotic entry of *Kmt2d*$^{+/\beta geo}$ NSCs (**Supplemental Figure I'**).

Pulse-labeling combined with marker-based imaging enables precise measurement of birth dates, i.e. mitotic division, of specific cell types. To resolve temporal dynamics of NPC differentiation in *Kmt2d*$^{+/\beta geo}$ and wild-type mice, we pulsed adult mice with EdU for a period of 2 weeks, during which time a subset of labeled DG cells is expected to reach the late NPC or immature neuron stage, characterized by the radial extension of a DCX$^+$ neuronal process from the cell body toward the hippocampal molecular layer. In contrast, a different subset of labeled cells bearing a NES$^+$ qRGL NSC-like process represents the population of cells that have not yet progressed beyond a stem-like state. Thus, by quantifying EdU-labeled cells exhibiting either a DCX$^+$ neuronal process (EdU$^+$/DCX$^+$) or a NES$^+$ qRGL NSC-like process (EdU$^+$/NES$^+$) (**Figure 5E, Supplementary Figure 7A**), one can compare relative differentiation states achieved by these cells, and a higher proportion of EdU$^+$/DCX$^+$ cells would indicate precocious differentiation. Indeed, while steady-state cell numbers in this experiment again showed overall decreases in both NES$^+$ qRGL NSCs and DCX$^+$ NPCs in *Kmt2d*$^{+/\beta geo}$ mice compared to wild-type (**Supplementary Figure 7A'**), among pulsed cells the *Kmt2d*$^{+/\beta geo}$ mice exhibited a higher fraction of EdU$^+$/DCX$^+$ immature neurons than *Kmt2d*$^{+/+}$ littermates (**Figure 5E'**). In other words, *Kmt2d*$^{+/\beta geo}$ mouse DG cells born in the preceding 2 weeks occupied a more advanced differentiation state than wild-type DG cells born in the same window.

Together, studies of adult neurogenesis in *Kmt2d*$^{+/\beta geo}$ mice suggest that neurodevelopmentally relevant *in vivo* consequences of KMT2D loss accompany cell cycle defects and transcriptional profiles similar to those expected from findings in our mouse and human *in vitro* models. We found reduced representation of adult DG NPCs beginning with the earliest NSC stages, suggesting baseline depletion of the adult-born NSC pool in the KS1 mouse model of ID. Furthermore, the demonstration of precocious differentiation *in vivo* supports our hypothesis that transcriptional perturbations due to KMT2D loss may lead to premature neuronal differentiation. Thus, changes in proliferation, cell cycle, gene expression, and neural differentiation due to KMT2D deficiency that we observed cell-autonomously *in vitro,* are recapitulated *in vivo* in the heterogeneous adult DG NPC niche of KS1 mice, providing a putative cellular mechanism of ID etiology in KS1.

bioRxiv preprint doi: https://doi.org/10.1101/484410; this version posted April 8, 2019. The copyright holder for this preprint (which was not certified by peer review) is the author/funder, who has granted bioRxiv a license to display the preprint in perpetuity. It is made available under aCC-BY-NC-ND 4.0 International license.

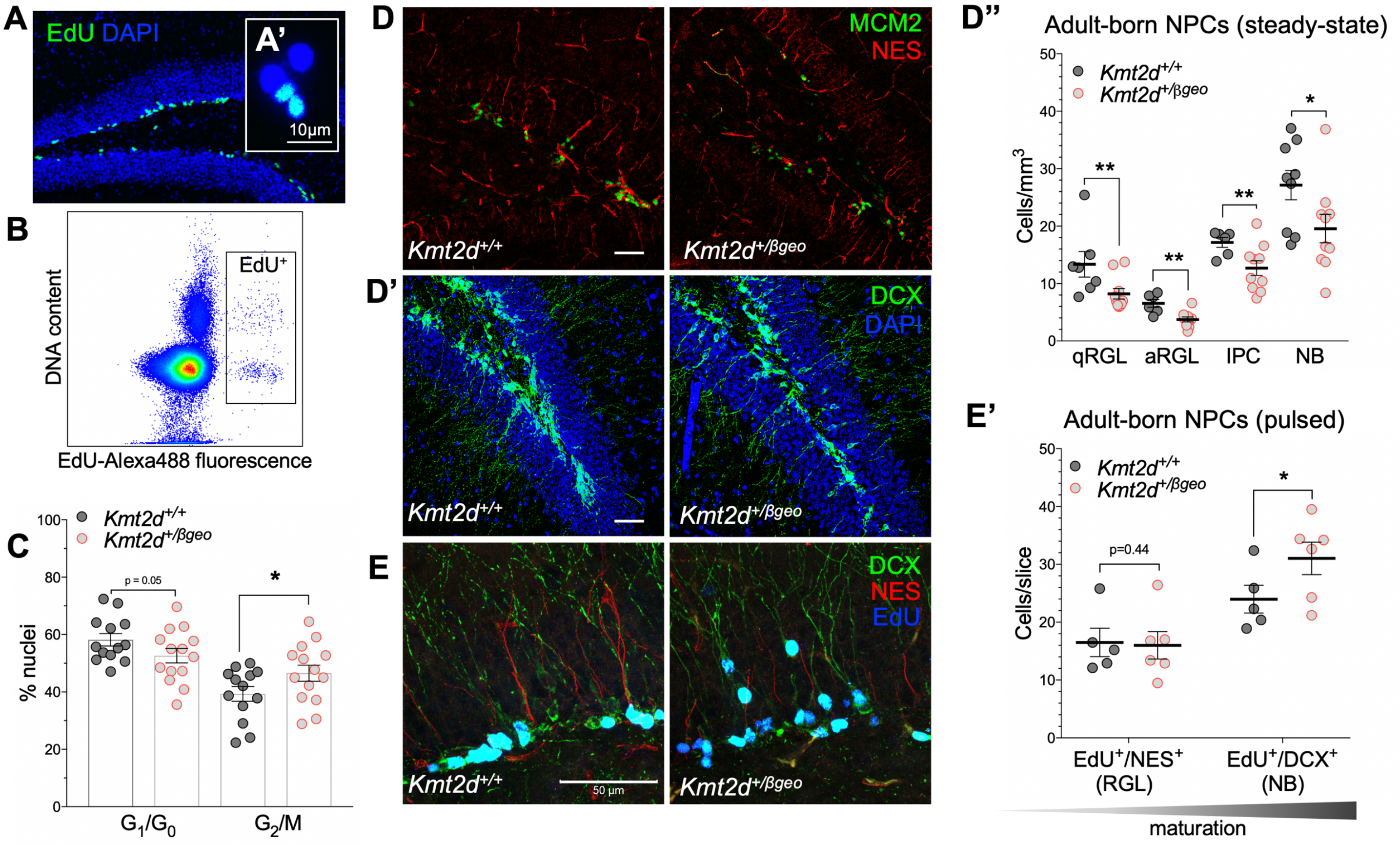

Figure 5. *In vivo* NSC depletion and precocious NPC differentiation in a mouse model of Kabuki syndrome. (**A**) Immunostaining of cycling, EdU-labeled DG cells and isolated nuclei from microdissected DG (**A'**) with flow cytometric purification (**B**) of labeled nuclei. (**C**) Cell cycle analysis of EdU$^+$ nuclei from *Kmt2d*$^{+/+}$ and *Kmt2d*$^{+/\beta geo}$ mice sampled 16 hours after EdU pulse, using DAPI fluorescence (13-14 mice per genotype). (**D-D''**) Representative immunostaining of steady-state neurogenesis markers in the dentate gyrus (DG) of adult *Kmt2d*$^{+/+}$ and *Kmt2d*$^{+/\beta geo}$ mice (6-10 mice per genotype, 7-10 slices per mouse). Earliest stages of nestin (NES)$^+$ radial glia-like (RGL) NSCs in either quiescent (MCM2$^-$) or activated (MCM2$^+$) states (qRGL and aRGL, respectively), MCM2$^+$/NES$^-$ intermediate progenitor cells (IPCs) (**D**), and DCX$^+$ NPCs (**D'**). (**D''**) Quantification of qRGL, aRGL, IPC, and DCX$^+$ NPCs cell densities in adult *Kmt2d*$^{+/+}$ and *Kmt2d*$^{\beta/geo}$ mice. (**E**) Representative immunostaining from *Kmt2d*$^{+/+}$ and *Kmt2d*$^{+/\beta geo}$ mice (5-6 mice per genotype, 10 slices per mouse) of EdU pulse-labeled cells extending a NES$^+$ process (NSCs) or DCX$^+$ process (NPCs), with (**E'**) quantification of double-labeled cells. Bars indicate mean ± SEM. Asterisks indicate significance from control mean, Student's t-test (*p<0.05, **p<0.01, ***p<0.001).

bioRxiv preprint doi: https://doi.org/10.1101/484410; this version posted April 8, 2019. The copyright holder for this preprint (which was not certified by peer review) is the author/funder, who has granted bioRxiv a license to display the preprint in perpetuity. It is made available under aCC-BY-NC-ND 4.0 International license.

Discussion

The Mendelian disorders of epigenetic machinery (MDEM) are a major emerging cause of ID (2). In these congenital syndromes, mutations in genes encoding chromatin-modifying enzymes disrupt local chromatin states and gene expression, resulting in multisystem anomalies. Though individually rare, the MDEM provide valuable insights to the functional consequences of altered epigenetic states. The ID disorder KS1 is caused by mutations in the histone methyltransferase *KMT2D*, but mechanistic links to neurodevelopmental and cognitive consequences in patients have not been established. KS1 diagnoses are typically made after birth, but the inherent reversibility of chromatin modifications raises the possibility that a detailed understanding of KMT2D activity in neuronal cells could identify specific molecular targets for postnatal interventions in KS1 patients.

Here, we report that KMT2D-deficient human and mouse neurodevelopment models, *in vitro* and *in vivo*, demonstrate similar patterns of transcriptional suppression, proliferative defects, and precocious cellular differentiation. These phenotypes were cell-autonomous *in vitro*, suggesting that 1) chromatin and gene expression studies in neurogenic cell types could yield disease-relevant KMT2D targets and 2) these cellular models provide platforms for screening of novel therapeutic strategies or targeted manipulations. In this study, we perform extensive transcription and KMT2D profiling in these models and observe systematic suppression of hypoxia response pathways, particularly among HIF1A-regulated genes that are also directly KMT2D-bound in neuronal cells. Physically overlapping KMT2D- and HIF1A-bound genomic loci were observed even across different tissues, namely on gene promoters in neuronal and cardiac cells, raising the possibility of shared etiologies in embryonically distinct KS1-affected organ systems. Indeed, KMT2D-deficient neuronal cells, in contrast to isogenic wild-type cells, were unable to mount a characteristic hypoxia-inducible gene activation response when exposed to low-oxygen conditions, demonstrating oxygen sensing defects in KS1, and future studies could interrogate KS1 neuronal differentiation phenotypes upon targeted manipulations of oxygen sensing loci.

The implication of hypoxia-responsive expression defects in KS1 suggests clinical relevance of two recent neurodevelopmental findings. First, the adult hippocampal NPC niche harbors locally hypoxic, but dynamic microenvironments, and the hypoxic state positively influences NPC survival (32). Thus, compromised oxygen-sensing is expected to render NPCs particularly vulnerable to changes in oxygen pressure experienced by differentiating, migrating NPCs. Second, NPC maturation is coupled to a metabolic rewiring from glycolysis, in early NPCs, to oxidative phosphorylation in immature neurons. Zheng and colleagues (17) recently found this metabolic switch, marked by suppression of glycolytic genes (*Ldha, Hk2*), to be essential for neuronal maturation. We observed

bioRxiv preprint doi: https://doi.org/10.1101/484410; this version posted April 8, 2019. The copyright holder for this preprint (which was not certified by peer review) is the author/funder, who has granted bioRxiv a license to display the preprint in perpetuity. It is made available under aCC-BY-NC-ND 4.0 International license.

suppression of these and related genes in KS1 models, accompanied by upregulation of pro-neuronal differentiation genes, as well as precocious differentiation of pulsed adult DG NPCs and concomitant depletion of the NSC pool *in vivo* in the KS1 mouse model.

Analogous findings of premature activation of terminal differentiation genes, reduced proliferation, and precocious maturation in KMT2D-depleted keratinocytes were recently linked to disorganized epidermal stratification (10). Furthermore, in KMT2D-deficient cardiomyocytes, loss of H3K4me2 at KMT2D-bound hypoxia response genes associated with cell cycle and proliferative defects in heart development (6). In contrast, conditional KMT2D deletion in B cells conferred proliferative advantage and impaired cell maturation in a stage-dependent manner, despite significant up-regulation of differentiation genes (8, 9). Thus, while KMT2D's role in enhancer-mediated, cell type-specific gene expression during differentiation is well-established (11), phenotypic manifestations appear cell type- and stage-dependent. We now extend phenotypes of transcriptional perturbance, hypoxia response, cell cycle, proliferation, and premature differentiation to KMT2D-deficient neuronal contexts. Phenotypic concordance across tissues of disparate embryonic origin suggests that KMT2D targets important to KS1 phenotypes support basic cellular homeostatic functions related to housekeeping, energy production, and cell cycle progression, rather than genes with purely brain-specific function. Furthermore, we report concordant phenotypes both from nonsense *KMT2D* mutations (patient iPSCs and NPCs), and mutations limited to the KMT2D methyltransferase domain (HT22 neuronal cells, *Kmt2d*$^{+/\beta geo}$ mice), indicating that loss of either gene dosage or catalytic function of KMT2D can be pathogenic.

Present results indicate that the adult hippocampal neurogenesis defect, which we previously found to associate with visuospatial memory defects in *Kmt2d*$^{+/\beta geo}$ mice, originates from a depletion of the DG NSC pool itself rather than from stalling at any particular cell type transition. In fact, despite having fewer NPCs overall, we observed the *Kmt2d*$^{+/\beta geo}$ NPC population to occupy a more advanced maturation state than that of wild-type littermates. While adult-born NPCs comprise a small fraction of the adult hippocampus, they wield an outsized influence on DG networks which, strikingly, extends even to the contralateral hippocampus in promoting visuospatial memory ability (33). This bilateral, network-mediated performance improvement was abolished upon transient silencing of young, but not older, adult-born DG NPCs, suggesting that NPC maturation rates and cognitive effects are coupled (33). Such studies increase the likelihood that precocious differentiation, in the context of developing neurons, could measurably impact visuospatial memory. Furthermore, multispecies comparisons demonstrate that measured decreases in neurogenesis rates are consistent with accelerated neuronal maturation rates across the lifespan (34).

bioRxiv preprint doi: https://doi.org/10.1101/484410; this version posted April 8, 2019. The copyright holder for this preprint (which was not certified by peer review) is the author/funder, who has granted bioRxiv a license to display the preprint in perpetuity. It is made available under aCC-BY-NC-ND 4.0 International license.

The apparent paradox of increased HIF1A activation, despite blunted hypoxia-responsive expression in *Kmt2d*$^{+/\Delta}$ and *Kmt2d*$^{\Delta/\Delta}$ neuronal cells raises two possibilities. First, chronic HIF activity may reflect cellular compensatory efforts in the absence of negative feedback from hypoxia gene induction. In this case, heterochromatic environments at HIF-binding genes could prevent induction. Alternatively, cellular oxygen sensing could be coupled to chromatin states and gene expression in a HIF-independent manner. A pair of independent studies recently discovered direct oxygen sensing by KDM6A/UTX, the H3K27 demethylase lost in KS2 patients, as well as the H3K4/H3K36 demethylase 5A (KDM5A), directly producing HIF-independent changes in chromatin states, cell differentiation, and cell fate (35, 36). Specifically, independent findings of upregulated histone methylation at H3K4, H3K27, H3K9, and H3K36 in hypoxia, linked directly to cell maturation in widespread cell types, suggest that KS-associated targets are unusually vulnerable to oxygen pressure changes, and support mechanistic links between our neuronal hypoxia response and differentiation findings. Remarkably, the latter study found that genes showing hypoxia-upregulated H3K4me3 peaks were significantly enriched for HIF targets, and these loci were almost exclusively in promoters, precisely where we observed KMT2D peaks to overlap HIF1A peaks. Strikingly, loss of KDM5A, whose activity opposes that of KMT2D at H3K4 sites, resulted in elevated hypoxia-responsive expression, i.e. an effect inversely proportional to the present KS1-associated transcriptional suppression of hypoxia-response genes such as *Klf10* and *Bnip3l.* A number of histone demethylases, and at least 33 chromatin modifiers in total, are known to impact hypoxia response genes, with 11 of these associating with developmental disease or cancers, yet KMT2D and other histone methyltransferases have not yet been implicated (37).

In summary, our findings suggest that KMT2D deficiency disrupts neurogenesis by negatively impacting stem cell maintenance functions including cell cycle progression, proliferation, and survival, with concomitant NSC depletion and precocious neuronal differentiation *in vivo*. Chromatin and expression profiling identified KMT2D- and HIF-regulated gene programs suppressed across KS1 model systems, which mechanistically link hypoxia pathways with phenotypes observed by us and others. We functionally demonstrate KMT2D-dependent neuronal hypoxia responses and *in vivo* neurodevelopmental disruptions predicted from our cellular work. Together, our findings support a model in which KMT2D loss transcriptionally suppresses oxygen sensing programs critical to early NPC maintenance, resulting in precocious differentiation and exhaustion of precursors required for adult hippocampal neurogenesis.

bioRxiv preprint doi: https://doi.org/10.1101/484410; this version posted April 8, 2019. The copyright holder for this preprint (which was not certified by peer review) is the author/funder, who has granted bioRxiv a license to display the preprint in perpetuity. It is made available under aCC-BY-NC-ND 4.0 International license.

Methods

Animals

The *Kmt2d*$^{+/\beta geo}$ allele (Mll2Gt(RRt024)Byg) was generated by Bay Genomics (University of California) through the random insertion of a gene trap vector. *Kmt2d*$^{+/\beta geo}$ mice were fully backcrossed to C57Bl/6 background over more than 10 generations in the Bjornsson lab, and are born roughly in expected Mendelian ratios when bred to wild-type. Animals were housed in a 14-hour light/10-hour dark cycle with free access to food and water. All experiments compare mutant mice against age- and sex-matched wild-type littermates.

Patient-derived iPSCs, NPCs, and fibroblasts

Media and reagents are listed (**Supplementary Table 10**). Skin biopsy fibroblasts were cultured from molecularly confirmed KS1 patients (KS1-1, KS1-3, KS1-4) of the JHU Epigenetics and Chromatin Clinic. Patient KS1-1 was consented for stem cell derivation and cells were reprogrammed using non-integrating Sendai virus vectors (CytoTune-iPS 2.0, ThermoFisher Scientific, Waltham, MA). 5 days post-induction, cells were transferred to mouse embryonic fibroblast (MEF) feeder plates in iPSC media and monitored for colony formation. 21 days post-induction, colonies were manually selected for optimal iPSC morphology and quality for propagation. Karyotype analysis by G-banding confirmed 46, XX normal female karyotype in KS1-1. Generation and characterization of healthy control lines (C3-1 and C1-2) has been previously described (27). Feeder MEFs were derived from E13.5 CF-1 mouse embryos and mitotically inactivated by irradiation. iPSCs were enzymatically passaged every 4-8 days using collagenase and mechanical dissociation. NPCs were induced from iPSCs as previously described (28). Briefly, we synergistically inhibited signaling of glycogen synthase kinase 3 (GSK3), transforming growth factor β (TGF-β), γ-secretase, and Notch signaling pathways using small molecules CHIR99021 (4 μM), SB431542 (3 μM), and Compound E (0.1 μM), in the presence of hLIF (10 ng/ml) and ROCK inhibitor (5 μM) for 7 days. NPCs were split with Accutase and propagated in neural induction medium in feeder-free conditions on a Matrigel.

CRISPR-Cas9 deletions

Media and reagents are listed (**Supplementary Table 10**). HT22 mouse hippocampal cells were obtained commercially (MilliporeSigma, Burlington, MA) and maintained in HT22 media (DMEM with 10% FBS, pen/strep, GlutaMAX). sgRNAs targeting two loci spanning the *Kmt2d* SET domain-encoding region, with cut sites in exon 52 and either exon 54 or intron 54, were designed and selected for on-target activity scores >90% (crispr.mit.edu, **Supplementary Table 10**), and integrated into

bioRxiv preprint doi: https://doi.org/10.1101/484410; this version posted April 8, 2019. The copyright holder for this preprint (which was not certified by peer review) is the author/funder, who has granted bioRxiv a license to display the preprint in perpetuity. It is made available under aCC-BY-NC-ND 4.0 International license.

Cas9 plasmid (pSpCas9BB-2A-puro v2.0 (PX459), Addgene, Watertown, MA). Plasmids were delivered to HT22 cells at 20% confluency using Lipofectamine 2000 according to manufacturer protocol. After puromycin selection, heterozygous and homozygous cells were clonally expanded and maintained in culture according to standard protocols. Targeted clone genotypes were verified by PCR (primers listed) and Sanger sequenced at the Johns Hopkins Genetic Resources Core Facility (GRCF). A subset of clones appearing heterozygous by PCR (upper and lower DNA bands of expected size) were found to bear strand invasion in the upper band (**Supplementary Figure 1B**) and were removed from analyses. One such line, mutant Clone 1, was thus grouped with homozygous clones 2 and 3 for analysis, as both alleles were targeted in all three clones. Subsequent cellular assays were performed using Sanger-verified heterozygous and homozygous lines (Figures 1 and 2).

RNA-seq in HT22 cells: library preparation

Cells were plated at equal density and sampled at 60% confluency. Total RNA was isolated from three biological replicates of *Kmt2d*$^{\Delta/\Delta}$ clones and *Kmt2d*$^{+/+}$ wild-type parental cells using Direct-Zol RNA MicroPrep (Zymo Research, Irvine, CA), and libraries were constructed in technical triplicate using NEBNext Poly(A) Magnetic Isolation Module and NEBNext UltraII RNA Library Prep Kit for Illumina (New England BioLabs, Ipswich, MA), with size selection by AMPure XP beads (Beckman Coulter, Brea, CA), according to manufacturer protocols. Library quantification and quality checks were done using KAPA Library Quantification Kit for Illumina (KAPA Biosystems, Wilmington, MA), High Sensitivity DNA Kit on BioAnalyzer (Agilent, Santa Clara, CA), and Qubit dsDNA HS Assay (Life Technologies, Carlsbad, CA). Paired end 50 bp reads were obtained for pooled libraries using Illumina HiSeq 2500 at the JHU GRCF High Throughput Sequencing Center.

RNA-seq in HT22 cells: data analysis

Sequencing reads were pseudoaligned to the mouse reference transcriptome (GRCm38) and transcript abundances were subsequently quantified using Salmon (38). We then used the tximport R package (39) to convert the transcript abundances into normalized gene-level counts, by setting the “countsFromAbundance” parameter equal to “lengthScaledTPM”. Next, we used the edgeR (40) and limma (41) R packages to log2 transform these gene-level counts, estimate the mean-variance relationship, and calculate weights for each observation. In order to account for the correlation between technical replicates of the same clone when performing the differential analysis, we fit a mixed linear model, using the function “duplicateCorrelation” from the statmod R package (42) to block on clone. The differential analysis was then performed using the limma R package. Differentially

bioRxiv preprint doi: https://doi.org/10.1101/484410; this version posted April 8, 2019. The copyright holder for this preprint (which was not certified by peer review) is the author/funder, who has granted bioRxiv a license to display the preprint in perpetuity. It is made available under aCC-BY-NC-ND 4.0 International license.

expressed genes were called with 0.05 as the cutoff for the False Discovery Rate (FDR). When performing the principal component analysis, transcript abundances were first converted into gene-level counts using the tximport R package, with the "countsFromAbundance" parameter equal to "no". Then, we applied a variance stabilizing transformation to these gene-level counts using the "vst" function from the DESeq2 R package (43) with the parameter "blind" set to "TRUE", and subsequently estimated the principal components using the 1000 most variable genes.

scRNA-seq: library preparation

NPCs were induced in parallel from each iPSC line (KS1-1, C1-2, C3-1) under identical conditions, and passaged three times before sampling. iPSCs were detached from MEF feeders using collagenase (200 units/ml). iPSCs and NPCs were dissociated to single-cell suspension using Accutase. Cell counts and viability were analyzed using Countess II Automated Cell Counter (ThermoFisher Scientific). scRNA-seq libraries were created with Chromium Single Cell 3' Library & Gel Bead Kit v2 (10x Genomics) according to manufacturer protocol. Targeted cell recovery for each sample was 5,000 cells. Sufficient cDNA for library construction was achieved using 20 amplification cycles for iPSC libraries and 16 cycles for NPC libraries. Sample indexing was achieved using 11 PCR cycles for iPSC libraries and 5 cycles for NPC libraries. scRNA-seq libraries were sequenced using Illumina NextSeq 500.

scRNA-seq: data analysis

Sequencing output was processed through the Cell Ranger 2.1.0 preprocessing pipeline using default parameters with the exception of --expect-cells=5000 for `cellranger count` and --normalize=none for `cellranger aggr`. Reads were quantified against hg19 using the 10x reference genome and transcriptome builds (refdata-cellranger-GRCh38-1.2.0). The aggregated raw count matrix was then used as input for the Monocle2 single-cell RNAseq framework. Differential gene expression analysis was performed on all NPCs and iPSCs with respect to genotype (KS1 patient vs healthy control) and was performed using the Monocle2 (44) likelihood ratio test (0.1% FDR, Monocle2 LRT, Benjamini-Hochberg corrected) with `num_genes_expressed` added as a nuisance parameter to both the full and reduced models. The directionality of the differential gene test was determined by calculating the mean gene expression across all KS1 patient-derived and healthy control cells respectively, evaluating the relative fold change. High-variance genes were selected as those with a positive residual to the estimated dispersion fit and a mean number of reads per cell >=0.0005. Cell cycle stage was determined by profiling cell cycle associated genes across all cells and assigning cell cycle state using

bioRxiv preprint doi: https://doi.org/10.1101/484410; this version posted April 8, 2019. The copyright holder for this preprint (which was not certified by peer review) is the author/funder, who has granted bioRxiv a license to display the preprint in perpetuity. It is made available under aCC-BY-NC-ND 4.0 International license.

the R/Bioconductor package scran (45). Dimensionality reduction and visualization was performed via UMAP (29) on the log10(counts + 1) of the high variance genes in the NPC dataset. The first 10 principal components were used as input for UMAP using the default parameters of the R/CRAN package umap. Cells were assigned to clusters using Monocle2's implementation of the louvain community detection algorithm. Learned clusters were then aggregated by hand based on marker gene expression into three clusters ("Differentiating", "Transitioning", "Cycling"). Differential gene expression within clusters, and between genotypes was performed as described above. The "Differentiating" cluster was then segregated, and a smooth line was fitted using a linear regression. This line was determined to represent the direction of differentiation by examination of marker genes (**Supplemental Figure 5B-E''**). The residuals of this fit were then plotted and deciles were calculated containing equal number of cells along the axis of differentiation. The number of cells in each decile was then counted with respect to genotype.

ChIP-seq: library preparation

Kmt2d$^{+/+}$ and *Kmt2d*$^{\Delta/\Delta}$ HT22 cells were sampled at 70% confluency and processed for pull-down with ChIP-grade KMT2D antibody (Millipore Sigma) according to ENCODE guidelines. Sonicated, reverse-crosslinked chromatin served as input control. Briefly, ~300 million cells per cell line were crosslinked in 1% formaldehyde, quenched with 0.125 M glycine, and cell lysate supernatants were collected for immediate processing or snap-frozen for storage at -80°C. Nuclei diluted in 1 ml RIPA buffer were sonicated using Bioruptor (Diagenode, Denville, NJ) for 6 cycles of 5 minutes (60 seconds on/30 seconds off) in ice-cold water bath. Supernatants containing sheared chromatin were pre-cleared with Protein A Dynabeads (ThermoFisher Scientific) and incubated overnight at 4°C with 8 μg KMT2D antibody. ChIP DNA was recovered by Dynabead incubation (overnight at 4°C plus 6 hours at room temperature) before 6 sequential salt washes of increasing stringency, then eluted and reverse crosslinked overnight at 65°C. DNA was purified using DNA Clean and Concentrator (Zymo Research) and quantified using High Sensitivity DNA Kit on BioAnalyzer (Agilent), and Qubit dsDNA HS Assay (Life Technologies). DNA libraries were constructed using NEBNext UltraII DNA Library Prep Kit for Illumina (New England BioLabs) and quantified using KAPA Library Quantification Kit for Illumina (KAPA Biosystems). Paired end 75 bp reads were obtained for pooled libraries using Illumina HiSeq 2500 at the JHU GRCF High Throughput Sequencing Center.

ChIP-seq: data analysis

bioRxiv preprint doi: https://doi.org/10.1101/484410; this version posted April 8, 2019. The copyright holder for this preprint (which was not certified by peer review) is the author/funder, who has granted bioRxiv a license to display the preprint in perpetuity. It is made available under aCC-BY-NC-ND 4.0 International license.

Sequencing reads were aligned to the mouse reference genome (mm10) using Bowtie2 (46). Then, duplicate reads were removed with the function MarkDuplicates from Picard (http://broadinstitute.github.io/picard/). Peaks were subsequently called using MACS2 (47), with the "keep-dup" parameter equal to "all". After peak calling, we excluded all peaks that overlapped with blacklisted regions provided by ENCODE (https://sites.google.com/site/anshulkundaje/projects/blacklists). To identify genes whose promoters were bound by KMT2D, we defined promoters as 10kb regions centered around the TSS. We obtained TSS coordinates using the "exonsBy" function from the "TxDb.Mmusculus.UCSC.mm10.knownGene" R package (Team BC, Maintainer BP (2018). TxDb.Mmusculus.UCSC.mm10.knownGene: Annotation package for TxDb object(s). R package version 3.4.4.), with the "by" parameter equal to "gene".

Purification of EdU$^+$ nuclei

Mice were given 150 mg/kg EdU by intraperitoneal injection and sampled after 16 hours. Dentate gyrus (DG) was micro-dissected in ice-cold PBS immediately following sacrifice by halothane inhalation. Total nuclei were purified as described (48) with addition of RNase inhibitor to all buffers (**Supplementary Table 10**). Briefly, bilateral DG from individual mice were dounce-homogenized in 1 ml lysis buffer and layered above a sucrose gradient for ultracentrifugation at 28,600 RPM for 2 hours at 4°C. Supernatant was aspirated and nuclei were resuspended in Click-iT EdU AlexaFluor-488 Flow Cytometry Kit buffer with addition of RNAse inhibitor, and incubated 30 minutes at room temperature. Samples were passed through 40 µm filter, stained with 1 µg/ml DAPI, and kept on ice before sorting. Nuclear lysates processed identically from non-EdU-injected mice served as negative controls during sorting with Beckman Coulter MoFlo Cell Sorter as above. Cell cycle analysis by DNA content was performed with analysis gates discriminating 2N and 4N cells by DAPI fluorescence.

RNA-seq: EdU$^+$ nuclei

Purified EdU$^+$ nuclei from *Kmt2d*$^{+/\beta geo}$ female mice (500 nuclei pooled from 3 mice) and sex- and age-matched littermates (500 nuclei pooled from 3 mice) were sorted into Smart-Seq 2 lysis buffer (2 µL Smart-Seq2 lysis buffer with RNase inhibitor, 1 µL oligo-dT primer, and 1 µL dNTPs), briefly spun by tabletop microcentrifuge, and snap-frozen on dry ice. Lysates were stored at -80°C until cDNA conversion. Nuclei were processed according to a modified Smart-seq2 protocol (49). Briefly, lysates were thawed to 4°C, heated to 72°C for 5 minutes, and immediately placed on ice. Template-switching first-strand cDNA synthesis was performed using a 5'-biotinylated TSO oligo. cDNAs were amplified using 20 cycles of KAPA HiFi PCR and 5'-biotinylated ISPCR primer. Amplified cDNA was

bioRxiv preprint doi: https://doi.org/10.1101/484410; this version posted April 8, 2019. The copyright holder for this preprint (which was not certified by peer review) is the author/funder, who has granted bioRxiv a license to display the preprint in perpetuity. It is made available under aCC-BY-NC-ND 4.0 International license.

cleaned using 1:1 ratio of Ampure XP beads and approximately 250 pg was input to a one-quarter-sized Nextera XT tagmentation reaction. Tagmented fragments were amplified for 12 enrichment cycles and dual indexes were added to each well to uniquely label each library. Concentrations were assessed with Quant-iT PicoGreen dsDNA Reagent (Invitrogen) and samples were diluted to ~2nM and pooled. Pooled libraries were sequenced on the Illumina HiSeq 2500 platform to a target mean depth of ~8 x 105 bp paired-end fragments per cycle at the Johns Hopkins Genetic Resources Core Facility. For all libraries, paired-end reads were aligned to the mouse reference genome (mm10) using HISAT2 (50) with default parameters except: -p 8. Aligned reads from individual samples were quantified against a reference genome (GENCODE vM8) (51). Quantification was performed using cuffquant with default parameters and the following additional arguments: --no-update-check –p 8. Normalized expression estimates across all samples were obtained using cuffnorm with default parameters (52).

RT-qPCR

Total RNA was isolated by RNeasy Mini (Qiagen, Venlo, Netherlands) and cDNA libraries were constructed with High-Capacity cDNA Reverse Transcription Kit (Applied Biosystems, Foster City, CA) according to manufacturer protocols. Experiments were performed in technical triplicate and no explicit power analysis was used to determine sample numbers. Probes were from Taqman (ThermoFisher Scientific, **Supplementary Table 10**).

Immunostaining, confocal imaging, and processing

Coronal brain sections (30 μm) through the entire dentate gyrus (every sixth slice) were maintained in serial order. Brains were paraformaldehyde-fixed by transcardial perfusion and post-fixed in 4% PFA overnight at 4°C before cryoprotection by sequential overnight incubations at 4°C with sucrose concentrations of 10%, 20% and 30% in phosphate buffer. Brains were sectioned by cryostat (Leica, Wetzlar, Germany), directly mounted to charged slides, and stored at -80°C. Antigen retrieval (DakoCytomation) was performed at 95°C for 20 minutes. After blocking, overnight incubation at 4°C in primary antibodies (**Supplementary Table 10**) was followed by 2-hour room temperature incubation with AlexaFluor-conjugated secondary antibodies at 1:500 dilution. Blocking buffer of 0.1% Triton X-100 in TBS contained 6% serum matched to the host species of secondary antibody. Tiled, z-stacked images were acquired using an inverted Zeiss LSM780 FCS AxioObserver confocal microscope and Zen software (Zeiss) to encompass the entire GCL area of each section using 10X, 20X, or 40X objective. Images were quantified using Imaris (BitPlane, Zurich, Switzerland) by experimenters

bioRxiv preprint doi: https://doi.org/10.1101/484410; this version posted April 8, 2019. The copyright holder for this preprint (which was not certified by peer review) is the author/funder, who has granted bioRxiv a license to display the preprint in perpetuity. It is made available under aCC-BY-NC-ND 4.0 International license.

blinded to genotype. Cell counts for each GCL slice analyzed were corrected by the total GCL area multiplied by z-thickness of the image, and expressed as cells/mm^3. For pulse-label experiments, mice were injected with 150 mg/kg EdU in saline every 48 hours from P41-P54 and sampled on P55 to be processed for staining as before. DCX$^+$ neuroblast distance from SGZ plane was measured in Fiji (NIH, Bethesda, MD). No explicit power analysis was used to determine sample numbers. iPSCs and NPCs were plated at equal density and fixed with 4% PFA for 15 minutes at room temperature, blocked and permeabilized with 0.25% Triton X-100 and 10% donkey serum in PBS, then stained for 1 hour at room temperature in primary antibodies and 1 hour at room temperature in secondary antibodies. iPSC and NPC images were acquired using EVOS FL Cell Imaging System (ThermoFisher Scientific) and analyzed using Fiji. HT22 cells were cultured on glass coverslips and stained and imaged as above using Zeiss LSM780.

FACS and analysis

Flow cytometric analysis was carried out using FACSverse instrument and FACSsuite software (BD Biosciences), and FACS was performed using Beckman Coulter MoFlo Cell Sorter with proper gate settings and doublet discrimination (**Supplemental Figure 3M, Supplemental Figure 6A**) at the Johns Hopkins Bloomberg School of Public Health Flow Cytometry Core. Cell samples containing at least 10,000 cells were analyzed from technical triplicate culture wells and analysis was performed in FlowJo v10 (Tree Star Inc, Ashland, OR). No explicit power analysis was used to determine sample numbers. Feeder-free iPSCs and NPCs, HT22 cells, or patient fibroblasts were enzymatically dissociated to single cell suspension. For antibody staining, cells were fixed with 4% PFA for 15 minutes at room temperature, blocked and permeabilized with 0.25% Triton X-100 and 10% donkey serum in PBS, and incubated with primary antibody for 30 minutes at room temperature, followed by 30 minutes in secondary antibody and 5 minutes in DAPI (1 μg/ml) for DNA content. Unstained and secondary-only samples served as control. For proliferation analysis, cells were sampled after 30-minute pulse of EdU (10 μM) using Click-iT EdU Flow Cytometry Assay (ThermoFisher Scientific) according to manufacturer protocol. Proteostat reagent (Enzo Life Sciences, Ann Arbor, MI), CellTrace Violet, and CellEvent caspase-3/7 reagent (ThermoFisher Scientific) were used according to manufacturer protocol. Proteasome inhibition was achieved using 5 μM MG-132 for 16 hours (Enzo Life Sciences). Cell cycle synchronization in HT22 cells or patient fibroblasts was achieved by treatment with 250 ng/ml nocodazole (Sigma, St. Louis, MO) for 18 hours before being released into complete media free of nocodazole for indicated time points.

bioRxiv preprint doi: https://doi.org/10.1101/484410; this version posted April 8, 2019. The copyright holder for this preprint (which was not certified by peer review) is the author/funder, who has granted bioRxiv a license to display the preprint in perpetuity. It is made available under aCC-BY-NC-ND 4.0 International license.

Magnetic Resonance Imaging (MRI)

3D T2-weighted MRI (9.4T) was performed in mouse brains following PFA perfusion-fixation by the JHU Department of Radiology Division of MR Research. Atlas-based volumetric analysis was performed in 25 brain regions, including hippocampus and olfactory bulb. Structural and ventricular volumes were corrected by total brain volume for analysis (DtiStudio). No explicit power analysis was used to determine sample numbers.

Statistics

Statistical analyses (excluding high-throughput data) were calculated using GraphPad Prism (version 7.0b), and p-values less than or equal to 0.05 were considered significant (*p<0.05, **p<0.01, ***p<0.001). Gene set enrichments were calculated by Overrepresentation analysis (ORA) with WebGestalt (53), or with Fisher’s Exact Test function using R version 3.5.2. Statistics for high-throughput experiments are described in Methods.

Study Approval

All experiments were performed using mouse protocols approved by the Animal Care and Use Committee of Johns Hopkins University School of Medicine and are in accordance with National Institutes of Health (NIH) guidelines for mouse care and handling. Informed consent for KS1 patient cell collection and iPSC derivation was obtained according to institutional IRB and ISCRO protocols approved by Johns Hopkins University School of Medicine.

Acknowledgments

Imaging was performed at the Johns Hopkins School of Medicine Microscope Facility with NIH support (S10OD016374). Karyotypes were analyzed by the Johns Hopkins Cytogenomics Laboratory with support from NICHD (1 U54 HD079123-01A1). We thank Michael Sherman for assistance with image quantification, Manisha Aggarwal for MRI analysis, Mark Sandusky for schematic designs. Hongjun Song and Kai Ge provided critical reagents and advice. Hal Dietz and Gregg Semenza provided indispensable guidance.

Conflict of interest statement

HTB is a consultant for Millennium Pharmaceuticals, otherwise authors declare no conflict of interest exists.

Funding

bioRxiv preprint doi: https://doi.org/10.1101/484410; this version posted April 8, 2019. The copyright holder for this preprint (which was not certified by peer review) is the author/funder, who has granted bioRxiv a license to display the preprint in perpetuity. It is made available under aCC-BY-NC-ND 4.0 International license.

HTB is funded through an Early Independence Award from the National Institutes of Health (NIH, DP5OD017877) and through a grant from the Louma G. Foundation.

Author contributions

GAC and HTB conceived the study; GAC and HTB wrote the manuscript; GAC, HNN, GC, JDR, LZ performed experiments; GAC, LB, JA, KDH and LG analyzed data.

Data availability

All high-throughput data is publicly available. For HT22 cell RNA-seq and ChIP-seq, and DG nuclei RNA-seq, see GEO Accession #GSE126167. For scRNA-seq data, see GEO Accession #GSE126027. Scripts for scRNA-seq analysis are available at https://github.com/Jaugust7/Kabuki-Syndrome-scRNA-analysis.

bioRxiv preprint doi: https://doi.org/10.1101/484410; this version posted April 8, 2019. The copyright holder for this preprint (which was not certified by peer review) is the author/funder, who has granted bioRxiv a license to display the preprint in perpetuity. It is made available under aCC-BY-NC-ND 4.0 International license.

References

1. Schuettengruber B, Bourbon H-M, Di Croce L, Cavalli G. Genome regulation by polycomb and trithorax: 70 years and counting.. *Cell* 2017;171(1):34–57.
2. Bjornsson HT. The Mendelian disorders of the epigenetic machinery.. *Genome Res.* 2015;25(10):1473–1481.
3. Ng SB et al. Exome sequencing identifies MLL2 mutations as a cause of Kabuki syndrome.. *Nat. Genet.* 2010;42(9):790–793.
4. Miyake N et al. KDM 6 A Point Mutations Cause K abuki Syndrome.. *Human mutation* 2013;34(1):108–110.
5. Hannibal MC et al. Spectrum of MLL2 (ALR) mutations in 110 cases of Kabuki syndrome.. *Am. J. Med. Genet. A* 2011;155A(7):1511–1516.
6. Ang S-Y et al. KMT2D regulates specific programs in heart development via histone H3 lysine 4 di-methylation.. *Development* 2016;143(5):810–821.
7. Ortega-Molina A et al. The histone lysine methyltransferase KMT2D sustains a gene expression program that represses B cell lymphoma development.. *Nat. Med.* 2015;21(10):1199–1208.
8. Zhang J et al. Disruption of KMT2D perturbs germinal center B cell development and promotes lymphomagenesis.. *Nat. Med.* 2015;21(10):1190–1198.
9. Lee J-E et al. H3K4 mono- and di-methyltransferase MLL4 is required for enhancer activation during cell differentiation.. *Elife* 2013;2:e01503.
10. Lin-Shiao E et al. KMT2D regulates p63 target enhancers to coordinate epithelial homeostasis.. *Genes Dev.* 2018;32(2):181–193.
11. Froimchuk E, Jang Y, Ge K. Histone H3 lysine 4 methyltransferase KMT2D.. *Gene* 2017;627:337–342.
12. Bjornsson HT et al. Histone deacetylase inhibition rescues structural and functional brain deficits in a mouse model of Kabuki syndrome.. *Sci Transl Med* 2014;6(256):256ra135.
13. Boisgontier J et al. Anatomical and functional abnormalities on MRI in kabuki syndrome.. *Neuroimage Clin.* [published online ahead of print: November 19, 2018]; doi:10.1016/j.nicl.2018.11.020
14. Gonçalves JT, Schafer ST, Gage FH. Adult neurogenesis in the hippocampus: from stem cells to behavior.. *Cell* 2016;167(4):897–914.
15. Moreno-Jiménez EP et al. Adult hippocampal neurogenesis is abundant in neurologically healthy subjects and drops sharply in patients with Alzheimer's disease.. *Nat. Med.* [published online ahead of print: March 25, 2019]; doi:10.1038/s41591-019-0375-9
16. Berg DA et al. A common embryonic origin of stem cells drives developmental and adult neurogenesis.. *Cell* [published online ahead of print: March 13, 2019]; doi:10.1016/j.cell.2019.02.010
17. Zheng X et al. Metabolic reprogramming during neuronal differentiation from aerobic glycolysis to neuronal oxidative phosphorylation.. *Elife* 2016;5. doi:10.7554/eLife.13374
18. Mohyeldin A, Garzón-Muvdi T, Quiñones-Hinojosa A. Oxygen in stem cell biology: a critical component of the stem cell niche.. *Cell Stem Cell* 2010;7(2):150–161.
19. Morimoto BH, Koshland DE. Induction and expression of long- and short-term neurosecretory potentiation in a neural cell line.. *Neuron* 1990;5(6):875–880.
20. Wang C et al. Enhancer priming by H3K4 methyltransferase MLL4 controls cell fate transition.. *Proc. Natl. Acad. Sci. USA* 2016;113(42):11871–11876.
21. Guo C et al. Global identification of MLL2-targeted loci reveals MLL2's role in diverse signaling pathways.. *Proc. Natl. Acad. Sci. USA* 2012;109(43):17603–17608.
22. Semenza GL. HIF-1: mediator of physiological and pathophysiological responses to hypoxia.. *J. Appl. Physiol.* 2000;88(4):1474–1480.

bioRxiv preprint doi: https://doi.org/10.1101/484410; this version posted April 8, 2019. The copyright holder for this preprint (which was not certified by peer review) is the author/funder, who has granted bioRxiv a license to display the preprint in perpetuity. It is made available under aCC-BY-NC-ND 4.0 International license.

23. Guimarães-Camboa N et al. Hif1α represses cell stress pathways to allow proliferation of hypoxic fetal cardiomyocytes.. *Dev. Cell* 2015;33(5):507–521.
24. Benita Y et al. An integrative genomics approach identifies Hypoxia Inducible Factor-1 (HIF-1)-target genes that form the core response to hypoxia.. *Nucleic Acids Res.* 2009;37(14):4587–4602.
25. Sanz JH, Lipkin P, Rosenbaum K, Mahone EM. Developmental profile and trajectory of neuropsychological skills in a child with Kabuki syndrome: implications for assessment of syndromes associated with intellectual disability.. *Clin Neuropsychol* 2010;24(7):1181–1192.
26. Harris J, Mahone EM, Bjornsson HT. Molecularly confirmed Kabuki (Niikawa-Kuroki) syndrome patients demonstrate a specific cognitive profile with extensive visuospatial abnormalities.. *J. Intellect. Disabil. Res.* [published online ahead of print: February 14, 2019]; doi:10.1111/jir.12596
27. Wen Z et al. Synaptic dysregulation in a human iPS cell model of mental disorders.. *Nature* 2014;515(7527):414–418.
28. Li W et al. Rapid induction and long-term self-renewal of primitive neural precursors from human embryonic stem cells by small molecule inhibitors.. *Proc. Natl. Acad. Sci. USA* 2011;108(20):8299–8304.
29. McInnes L, Healy J, Saul N, Großberger L. UMAP: uniform manifold approximation and projection. *JOSS* 2018;3(29):861.
30. Benjamin JS et al. A ketogenic diet rescues hippocampal memory defects in a mouse model of Kabuki syndrome.. *Proc. Natl. Acad. Sci. USA* 2017;114(1):125–130.
31. Morris AM, Churchwell JC, Kesner RP, Gilbert PE. Selective lesions of the dentate gyrus produce disruptions in place learning for adjacent spatial locations.. *Neurobiol. Learn. Mem.* 2012;97(3):326–331.
32. Chatzi C, Schnell E, Westbrook GL. Localized hypoxia within the subgranular zone determines the early survival of newborn hippocampal granule cells.. *Elife* 2015;4:e08722.
33. Zhuo J-M et al. Young adult born neurons enhance hippocampal dependent performance via influences on bilateral networks.. *Elife* 2016;5. doi:10.7554/eLife.22429
34. Snyder JS. Recalibrating the relevance of adult neurogenesis.. *Trends Neurosci.* 2019;42(3):164–178.
35. Chakraborty AA et al. Histone demethylase KDM6A directly senses oxygen to control chromatin and cell fate.. *Science (80-.).* 2019;363(6432):1217–1222.
36. Batie M et al. Hypoxia induces rapid changes to histone methylation and reprograms chromatin.. *Science (80-.).* 2019;363(6432):1222–1226.
37. Luo W, Wang Y. Epigenetic regulators: multifunctional proteins modulating hypoxia-inducible factor-α protein stability and activity.. *Cell Mol. Life Sci.* 2018;75(6):1043–1056.
38. Patro R, Duggal G, Love MI, Irizarry RA, Kingsford C. Salmon provides fast and bias-aware quantification of transcript expression.. *Nat. Methods* 2017;14(4):417–419.
39. Soneson C, Love MI, Robinson MD. Differential analyses for RNA-seq: transcript-level estimates improve gene-level inferences. [version 2; peer review: 2 approved]. *F1000Res.* 2015;4:1521.
40. Robinson MD, McCarthy DJ, Smyth GK. edgeR: a Bioconductor package for differential expression analysis of digital gene expression data.. *Bioinformatics* 2010;26(1):139–140.
41. Ritchie ME et al. limma powers differential expression analyses for RNA-sequencing and microarray studies.. *Nucleic Acids Res.* 2015;43(7):e47.
42. Giner G, Smyth GK. Statmod: probability calculations for the inverse Gaussian distribution.. *arXiv preprint arXiv:1603.06687* 2016;
43. Love MI, Huber W, Anders S. Moderated estimation of fold change and dispersion for RNA-seq data with DESeq2.. *Genome Biol.* 2014;15(12):550.

bioRxiv preprint doi: https://doi.org/10.1101/484410; this version posted April 8, 2019. The copyright holder for this preprint (which was not certified by peer review) is the author/funder, who has granted bioRxiv a license to display the preprint in perpetuity. It is made available under aCC-BY-NC-ND 4.0 International license.

44. Trapnell C et al. The dynamics and regulators of cell fate decisions are revealed by pseudotemporal ordering of single cells.. *Nat. Biotechnol.* 2014;32(4):381–386.

45. Lun ATL, McCarthy DJ, Marioni JC. A step-by-step workflow for low-level analysis of single-cell RNA-seq data with Bioconductor. [version 2; peer review: 3 approved, 2 approved with reservations]. *F1000Res.* 2016;5:2122.

46. Langmead B, Salzberg SL. Fast gapped-read alignment with Bowtie 2.. *Nat. Methods* 2012;9(4):357–359.

47. Zhang Y et al. Model-based analysis of ChIP-Seq (MACS).. *Genome Biol.* 2008;9(9):R137.

48. Rizzardi L et al. Neuronal brain region-specific DNA methylation and chromatin accessibility are associated with neuropsychiatric disease heritability. *BioRxiv* [published online ahead of print: March 24, 2017]; doi:10.1101/120386

49. Picelli S et al. Smart-seq2 for sensitive full-length transcriptome profiling in single cells.. *Nat. Methods* 2013;10(11):1096–1098.

50. Kim D, Langmead B, Salzberg SL. HISAT: a fast spliced aligner with low memory requirements.. *Nat. Methods* 2015;12(4):357–360.

51. Mudge JM, Harrow J. Creating reference gene annotation for the mouse C57BL6/J genome assembly.. *Mamm. Genome* 2015;26(9–10):366–378.

52. Trapnell C et al. Differential gene and transcript expression analysis of RNA-seq experiments with TopHat and Cufflinks.. *Nat. Protoc.* 2012;7(3):562–578.

53. Wang J, Vasaikar S, Shi Z, Greer M, Zhang B. WebGestalt 2017: a more comprehensive, powerful, flexible and interactive gene set enrichment analysis toolkit.. *Nucleic Acids Res.* 2017;45(W1):W130–W137.

bioRxiv preprint doi: https://doi.org/10.1101/484410; this version posted April 8, 2019. The copyright holder for this preprint (which was not certified by peer review) is the author/funder, who has granted bioRxiv a license to display the preprint in perpetuity. It is made available under aCC-BY-NC-ND 4.0 International license.

Figures and Table

Figure 1. Genetic ablation of the *Kmt2d* SET methyltransferase domain disrupts cell proliferation and cell cycle in a cell-autonomous manner.

Figure 2. Suppressed transcription of KMT2D- and HIF-regulated hypoxia response genes upon loss of the *Kmt2d* SET methyltransferase domain in neuronal cells.

Figure 3. KS1 patient-derived cells recapitulate KMT2D-associated defects in proliferation and cell cycle.

Figure 4. Transcriptional suppression of metabolic genes in cycling cells, and hallmarks of precocious neuronal differentiation in KS1 patient-derived NPCs.

Figure 5. *In vivo* NSC depletion and precocious NPC differentiation in a mouse model of Kabuki syndrome.

Table 1: KMT2D-bound genes that are differentially expressed in *Kmt2d*$^{\Delta/\Delta}$ neuronal cells.

Supplemental Figures

Supplementary Figure 1: CRISPR-targeted HT22 cells

Supplementary Figure 2: HT22 cell RNA-seq and ChIP-seq analysis

Supplementary Figure 3: iPSC and NPC validations and phenotyping

Supplementary Figure 4: iPSC and NPC single-cell RNA-seq analysis

Supplementary Figure 5. Stratified scRNA-seq analysis of NPCs

Supplementary Figure 6: Adult neurogenesis phenotypes in *Kmt2d*$^{+/\beta geo}$ mice

Supplementary Figure 7: Pulse-labeling to birth-date adult-born NPCs *in vivo*

Supplemental Tables

Supplementary Table 1: Differentially expressed genes in HT22 cells (*Kmt2d*$^{+/+}$ versus *Kmt2d*$^{\Delta/\Delta}$)

Supplementary Table 2: KMT2D ChIP-seq peaks in HT22 cells (*Kmt2d*$^{+/+}$ cells)

Supplementary Table 3: KMT2D-bound genes in HT22 cells (*Kmt2d*$^{+/+}$ cells)

Supplementary Table 4: Differentially expressed genes in iPSCs (KS1 versus controls)

Supplementary Table 5: Differentially expressed genes in NPCs (KS1 versus controls)

Supplementary Table 6: Intersected gene sets of iPSCs and NPCs

Supplementary Table 7: Differentially expressed genes in NPCs (stratified by subsets)

Supplementary Table 8: Differentially expressed genes in EdU^{+} DG nuclei of *Kmt2d*$^{+/\beta geo}$ mice

Supplementary Table 9: MRI volumetric comparisons in wild-type and *Kmt2d*$^{+/\beta geo}$ mice

Supplementary Table 10: Reagents

bioRxiv preprint doi: https://doi.org/10.1101/484410; this version posted April 8, 2019. The copyright holder for this preprint (which was not certified by peer review) is the author/funder, who has granted bioRxiv a license to display the preprint in perpetuity. It is made available under aCC-BY-NC-ND 4.0 International license.

Fold change	**Number of genes**	**Genes**
0 to 1.1	11	***Dazap1***, *Psmc2*, *Eif3b*, ***Washc4***, *Ran*, ***Lrpprc***, *Imp4**, *Sf3a2**, *Bend3*, ***Hspd1****, *Dusp4*
-1 to 0	37	*Pik3ip1**, *Ssc5d*, *Plekha1*, *Tinagl1**, *Slc29a1*, *Rras*, *Nudt18*, *Slc25a29*, *F3*, *Pgpep1*, *Lrrn4cl*, *Gpr146*, ***Aldoa****, *Dbp*, ***Cpq***, *Pkm*, *Socs3*, *Map3k14**, *Rdm1*, ***Rara***, *Nfkbia**, ***Klf10****, ***Tob1***, *Irf2bp2*, *Fosl2*, ***Ddit4****, *Trim47*, *Btbd1*, *Plin2*, *Mxra8*, *Spg20*, ***Cited2****, *S100a11*, *Il34*, ***Bnip3l****, *Nfil3**, *Shb*
-2 to -1	16	*Ccl9*, *Crip2*, *Msln*, ***Cp****, *Scx*, *Klhl30**, *Vdr**, *Tnfsf13*, *Fcgr4*, *Emilin1**, *Oaf*, *Aqp1*, *C1qtnf1*, *Baalc*, *Macrod1*, *Fblim1*
-3 to -2	8	*Ly6c1*, *Ly6a*, *Lctl*, *Plin4*, *Angptl4**, *Tns4*, *Pkp3*, *Igf1**
-5 to -3	2	*Gjb4**, *Mfap4*

Table 1: **KMT2D-bound genes that are differentially expressed in *Kmt2d*$^{\Delta/\Delta}$ neuronal cells.** Positive fold changes (0 to 1.1) indicate genes up-regulated and KMT2D-bound. Negative fold changes (-5 to 0) indicate genes down-regulated and KMT2D-bound. *previously described KMT2D target genes (7, 21), **bold** genes having experimentally validated HIF1A binding in the promoter (24).

bioRxiv preprint doi: https://doi.org/10.1101/484410; this version posted April 8, 2019. The copyright holder for this preprint (which was not certified by peer review) is the author/funder, who has granted bioRxiv a license to display the preprint in perpetuity. It is made available under aCC-BY-NC-ND 4.0 International license.

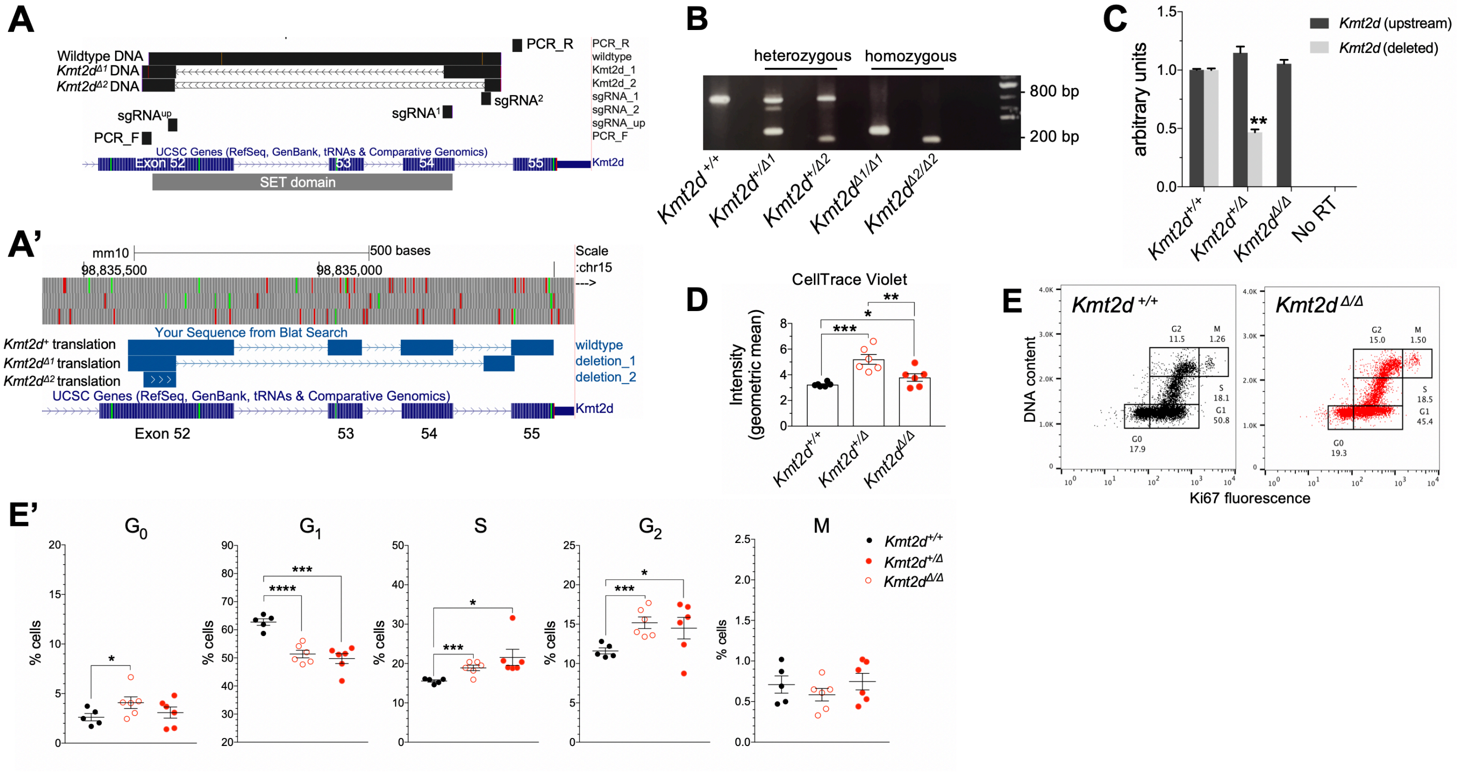

Supplementary Figure 1. CRISPR-targeted HT22 cells. (**A**) Sanger-sequenced DNA of wild-type (*Kmt2d*$^{+}$) and targeted (*Kmt2d*$^{\Delta}$) alleles in HT22 cells, mapped with sgRNAs and PCR primers, to *Kmt2d* locus (mm10) on chromosome 15. (**A'**) Mapping of Sanger-sequenced DNA after *in silico* translation to predict amino acid sequences illustrates premature termination codons (PTC) created in *Kmt2d*$^{\Delta 1}$ and *Kmt2d*$^{\Delta 2}$ alleles. (**B**) PCR with probes flanking sgRNA cut sites identifies experimental cell lines (*Kmt2d*$^{+/\Delta}$ and *Kmt2d*$^{\Delta/\Delta}$) compared to wild-type (*Kmt2d*$^{+/+}$). (**C**) RT-qPCR analysis of mRNA using probes spanning upstream exons (15-16) or exons within the deletion site (53-54). (**D**) CellTrace fluorescence intensities after 72 hours of proliferation analysis in HT22 cells. Increased intensity indicates less dye dilution, i.e. fewer cell divisions. (**E**) Cell cycle gating by flow cytometric analysis using Ki67 and DAPI to discriminate individual stages (G_0, G_1, S, G_2, M) in *Kmt2d*$^{+/+}$ and *Kmt2d*$^{\Delta/\Delta}$ cells, and (**E'**) quantification of each cycle phase.

bioRxiv preprint doi: https://doi.org/10.1101/484410; this version posted April 8, 2019. The copyright holder for this preprint (which was not certified by peer review) is the author/funder, who has granted bioRxiv a license to display the preprint in perpetuity. It is made available under aCC-BY-NC-ND 4.0 International license.

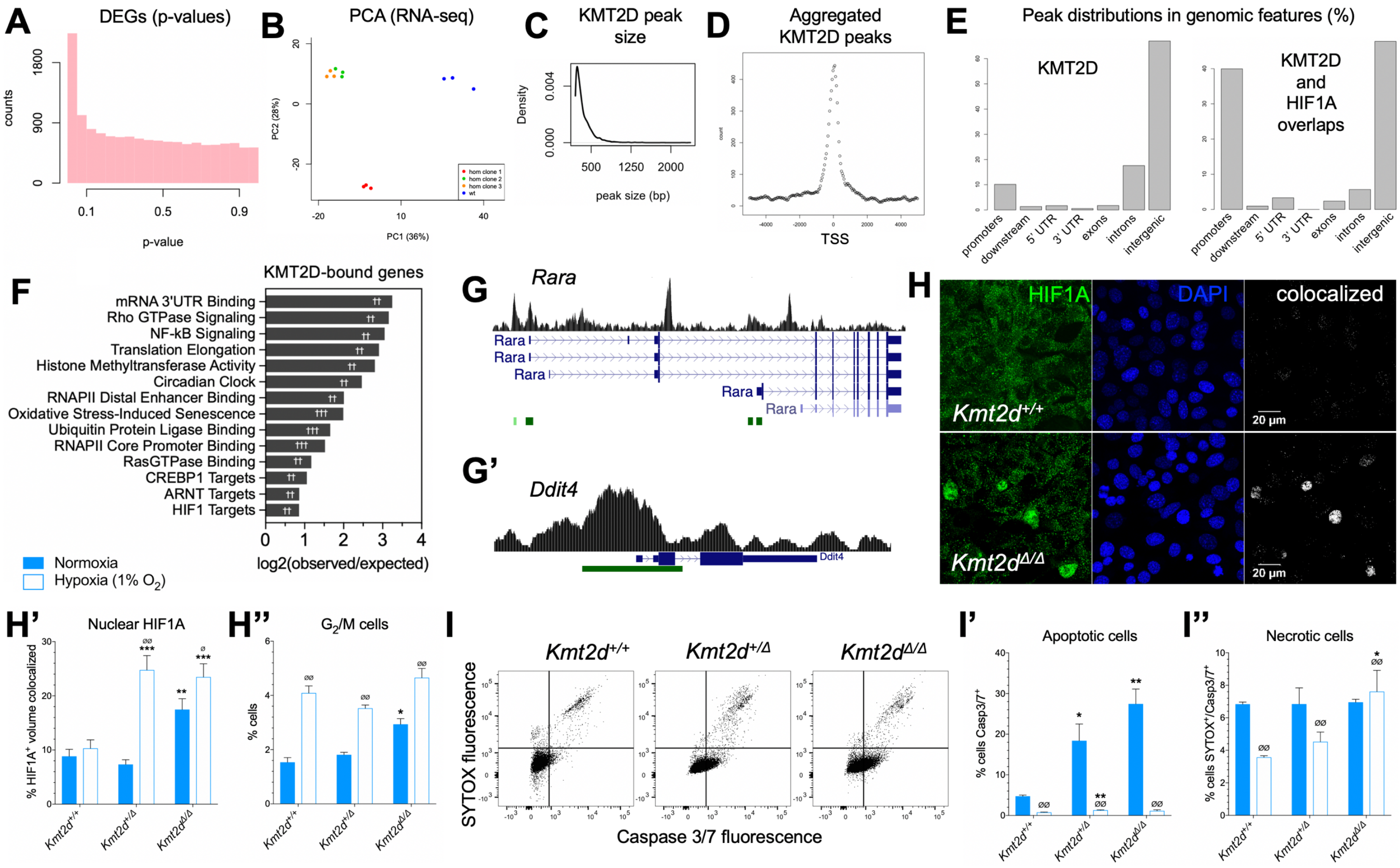

Supplementary Figure 2. HT22 cell RNA-seq and ChIP-seq analysis. (**A**) P-value distribution in *Kmt2d*$^{\Delta/\Delta}$ DEGs relative to wild-type indicate a well-calibrated test. (**B**) PCA visualizing clear expression differences in wild-type and *Kmt2d*$^{\Delta/\Delta}$ HT22 cells, illustrating separation of Clone 1 which bears strand invasion. (**C**) KMT2D ChIP-seq analysis comparing KMT2D peak density and peak size (bp) in wild-type HT22 cells. (**D**) Validation of expected KMT2D peak distributions about gene TSSs and (**E**) genomic features. (**F**) Gene networks showing highest fold change in enrichment among genes proximal to KMT2D peaks (<5 kb to promoter). (**G**) KMT2D peaks clustered at alternate TSSs of *Rara* gene and (**G'**) enhancer-like peaks at *Ddit4* gene. (**H**) HIF1A nuclear colocalization analysis (200-350 cells per condition). Representative Z-stacked confocal images of *Kmt2d*$^{+/+}$ and *Kmt2d*$^{\Delta/\Delta}$ cells under normoxic condition are shown with quantifications of colocalized HIF1A^{+} and DAPI^{+} voxels (**H'**), and %G$_2$/M phase cells measured by flow cytometry (12 wells per cell line) (**H''**) in all conditions. (**I**) Flow cytometric quantifications of cell death, with CellEvent fluorescence detecting caspase-3/7-mediated peptide cleavage in apoptotic cells (**I'**), and SYTOX reagent for necrotic cells (**I''**) (3-6 wells per cell line). Bars indicate mean ± SEM, Student's t-test (*p<0.05, **p<0.01, ***p<0.001). Fisher's Exact Test († FDR<0.05, †† FDR<0.01, ††† FDR<0.001).

bioRxiv preprint doi: https://doi.org/10.1101/484410; this version posted April 8, 2019. The copyright holder for this preprint (which was not certified by peer review) is the author/funder, who has granted bioRxiv a license to display the preprint in perpetuity. It is made available under aCC-BY-NC-ND 4.0 International license.

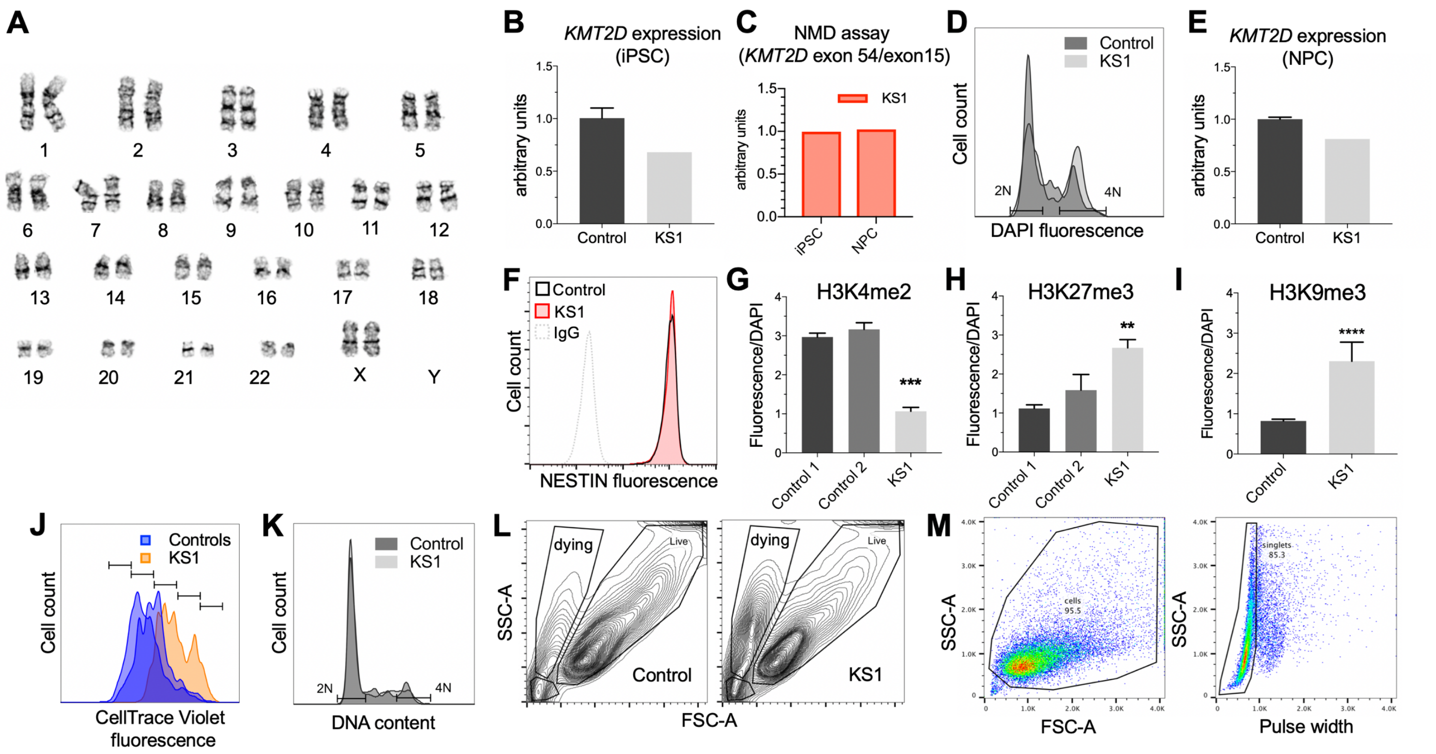

Supplementary Figure 3. iPSC and NPC line validations and additional phenotyping. (**A**) 46, XX normal female karyotype in KS1-1 iPSCs. (**B**) RT-qPCR analysis of *KMT2D* (exon 15) expression in KS1 iPSCs compared to two healthy control iPSC lines (C1-2 and C3-1), measured in technical triplicate. (**C**) RT-qPCR demonstrating equivalent exonic ratios of *KMT2D* exon 15 to exon 54, measured in technical triplicate, consistent with NMD of the entire transcript. (**D**) Flow cytometric analysis of DNA content by DAPI fluorescence in iPSCs. (**E**) RT-qPCR analysis of *KMT2D* (exon 15) expression in NPCs derived from the KS1 and control iPSC lines, measured in technical triplicate. (**F**) Flow cytometric analysis of NESTIN fluorescence intensity in KS1 and control NPCs. (**G-I**) Immunofluorescence imaging analysis of open chromatin mark H3K4me2 (**G**) and closed chromatin marks H3K27me3 (**H**) and H3K9me3 (**I**) in KS1 and control NPCs (9 images per line). (**J**) CellTrace Violet generational tracking showing fewer divisions (i.e. higher dye intensity) in patient-derived NPCs over 72 hours. (**K**) Flow cytometric analysis of DNA content by DAPI fluorescence in NPCs. (**L**) Sample flow cytometric gating for detection of scatter profiles indicative of cell death-associated cellular condensation. (**M**) Representative gating of viable cells and doublet discrimination in immunofluorescence-based flow cytometric analyses of iPSCs and NPCs. Bars indicate mean ± SEM, Student's t-test (*p<0.05, **p<0.01, ***p<0.001).

bioRxiv preprint doi: https://doi.org/10.1101/484410; this version posted April 8, 2019. The copyright holder for this preprint (which was not certified by peer review) is the author/funder, who has granted bioRxiv a license to display the preprint in perpetuity. It is made available under aCC-BY-NC-ND 4.0 International license.

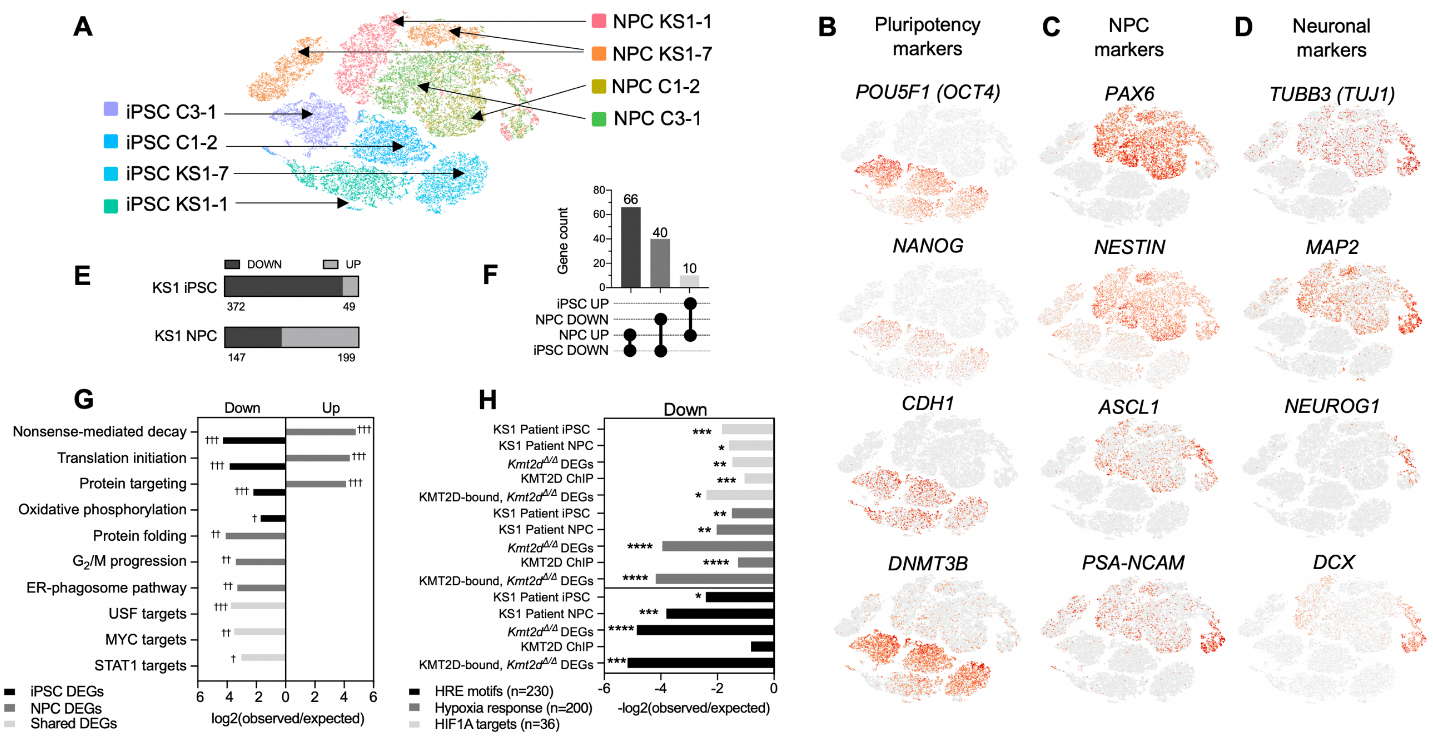

Supplementary Figure 4. iPSC and NPC single-cell RNA-seq analysis. (**A**) t-stochastic neighbor embedding (tSNE) representation of iPSC and NPC libraries sequenced on 10XGenomics platform. Cell clusters colored by cell type and Patient ID. iPSCs and NPCs derived from patient K1-7 were excluded from downstream analysis due to abnormal karyotype. (**B-D**) Representative tSNE of iPSC, NPC, and neuronal markers demonstrating expected cell identities and revealing a gradient of cell maturation. (**E**) Proportions of DEGs down- or up-regulated in KS1 patient iPSCs or NPCs compared to respective healthy controls, (**F**) DEG lists intersected for overlaps among down-regulated and up-regulated genes, and (**G**) Gene networks most enriched among differentially expressed genes (DEGs) in KS1 patient iPSCs and NPCs relative to respective healthy controls, and DEGs shared in both cell types. (**H**) Significant enrichments of Hypoxia Response genes, HIF1A Direct Target genes, and genes containing the Hypoxia Response Element (HRE) RCGTG motif among observed DEGs in KS1 Patient iPSCs, KS1 Patient NPCs, *Kmt2d*$^{\Delta/\Delta}$ HT22 cells, as well as KMT2D ChIP-seq genes in wild-type HT22 cells, and KMT2D-bound, down-regulated genes in *Kmt2d*$^{\Delta/\Delta}$ HT22 cells). Fisher's Exact Test (*p<0.05, **p<0.01, ***p<0.001, † FDR<0.05, †† FDR<0.01, ††† FDR<0.001).

bioRxiv preprint doi: https://doi.org/10.1101/484410; this version posted April 8, 2019. The copyright holder for this preprint (which was not certified by peer review) is the author/funder, who has granted bioRxiv a license to display the preprint in perpetuity. It is made available under aCC-BY-NC-ND 4.0 International license.

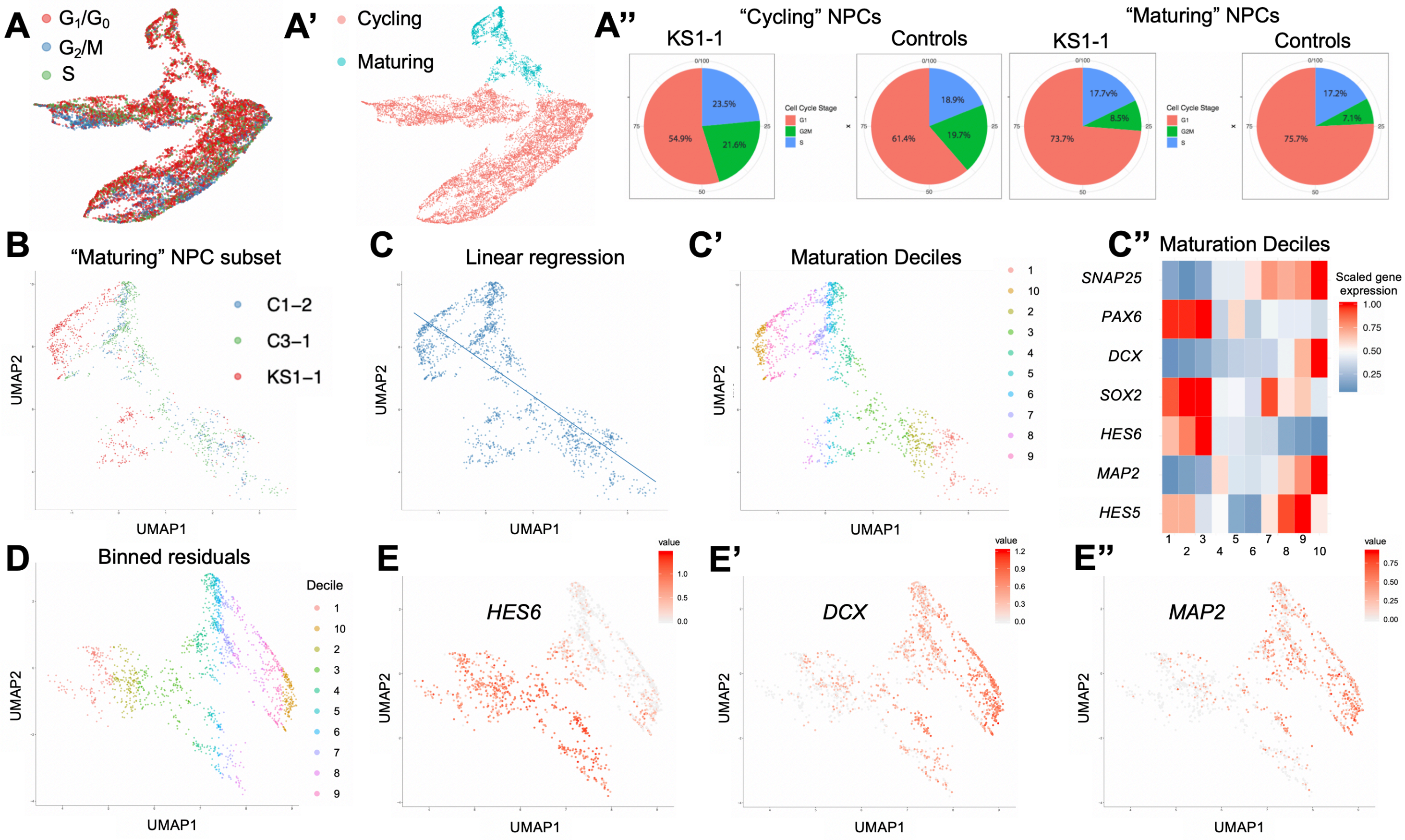

Supplementary Figure 5. Stratified scRNA-seq analysis of NPCs. (**A-A''**) Uniform Manifold Approximation Projection (UMAP) of single-cell NPC libraries partitioned by (**A**) cell cycle marker expression into subsets of G_1/G_0, S, and G_2/M cells, used for cycle phase-stratified differential expression analysis (**Supplementary Table 7**) to rule out confounding differences in cell cycle phase composition on NPC transcriptome comparisons. (**A'**) Subset of "Cycling" versus non-cycling, "Maturing" NPCs, which includes "Transitioning" and "Differentiating" cells as defined (**Figure 4B**), and (**A''**) UMAP-based cell cycle occupancies consistent with experimental FACS data (**Figure 3F**). (**B-C'**) UMAPs of the segregated population of Differentiating NPCs displaying (**B**) library patient ID's, (**C**) smooth linear regression fitted to define the maturation trajectory and (**C'**) binned deciles of progressively maturing cells along the regression. (**C''**) Relative expression of selected NPC markers defining directionality of the maturation trajectory. (**D**) Binned residuals used to calculate deciles containing equal number of cells along the axis of differentiation. (**E-E''**) Representative NPC marker expression plotted over binned residuals.

bioRxiv preprint doi: https://doi.org/10.1101/484410; this version posted April 8, 2019. The copyright holder for this preprint (which was not certified by peer review) is the author/funder, who has granted bioRxiv a license to display the preprint in perpetuity. It is made available under aCC-BY-NC-ND 4.0 International license.

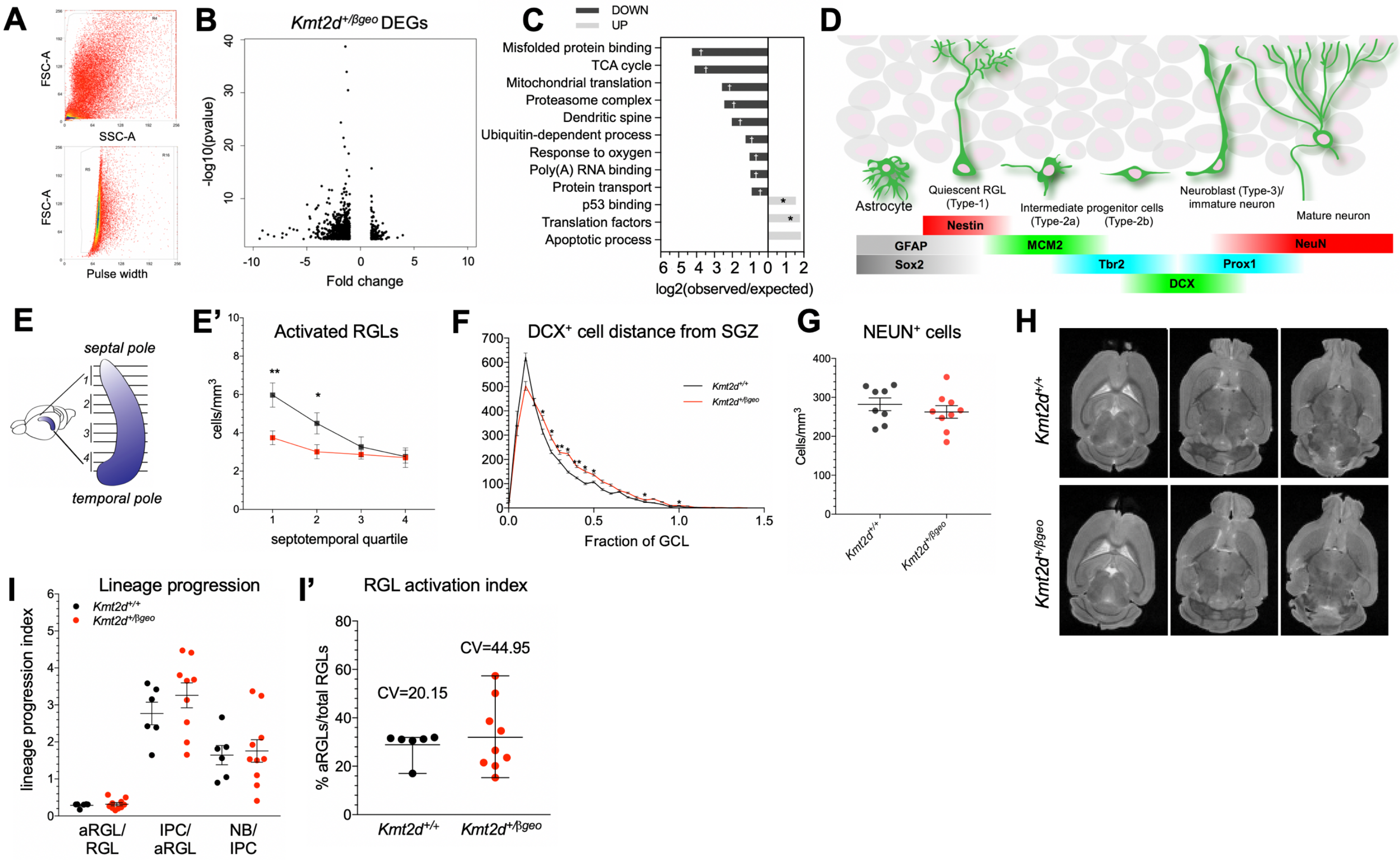

Supplementary Figure 6. Phenotyping of *Kmt2d*$^{+/\beta geo}$ mice. (**A**) Sample FACS gating for viable nuclei and doublet discrimination during purification of cycling EdU$^+$ nuclei purified from *Kmt2d*$^{+/+}$ and *Kmt2d*$^{+/\beta geo}$ mice at 16 hours post-EdU pulse for RNA-seq and cell cycle analysis. (**B**) RNA-seq analysis of differential gene expression in purified EdU$^+$ DG nuclei from *Kmt2d*$^{+/+}$ and *Kmt2d*$^{+/\beta geo}$ mice. (**C**) Gene networks most enriched among DEGs down- or up-regulated in *Kmt2d*$^{+/\beta geo}$ nuclei, showing transcriptional suppression of cellular metabolic pathways. (**D**) Schematic depicting marker expression during sequential stages of adult neurogenesis in the dentate gyrus (DG). (**E**) Serial ordering of perfusion-fixed brain slices enables anatomically-sequenced analysis of neurogenesis, for (**E'**) stratified quantification of aRGL density along the septotemporal axis of the DG in *Kmt2d*$^{+/+}$ and *Kmt2d*$^{+/\beta geo}$ mice, indicating preferential disruption at the septal DG, a brain region linked to visuospatial memory. (**F**) Quantification of DCX$^+$ cell body distance from SGZ plane in 8-week-old mice (9-10 mice per genotype, at least 100 cells per mouse). (**G**) Quantification of NEUN$^+$ cells in the granule cell layer (GCL) of 8-week-old mice (8-9 mice per genotype). (**H**) Sample images of T2-weighted MRI (9.4T) in PFA-fixed brains of female mice 4 months old. (**I-I'**) Comparison of lineage progression index, an approximation of expansion potential for each cell type transition, indicates absence of genotype-associated blockages at any particular cell-type transition analyzed, and (**I'**) increased Coefficient of Variance (CV) in RGL activation rates in *Kmt2d*$^{+/\beta geo}$ mice. Bars indicate mean ± SEM, Student's t-test (*p<0.05, **p<0.01, ***p<0.001). Fisher's Exact Test († FDR<0.05, †† FDR<0.01, ††† FDR<0.001).

bioRxiv preprint doi: https://doi.org/10.1101/484410; this version posted April 8, 2019. The copyright holder for this preprint (which was not certified by peer review) is the author/funder, who has granted bioRxiv a license to display the preprint in perpetuity. It is made available under aCC-BY-NC-ND 4.0 International license.

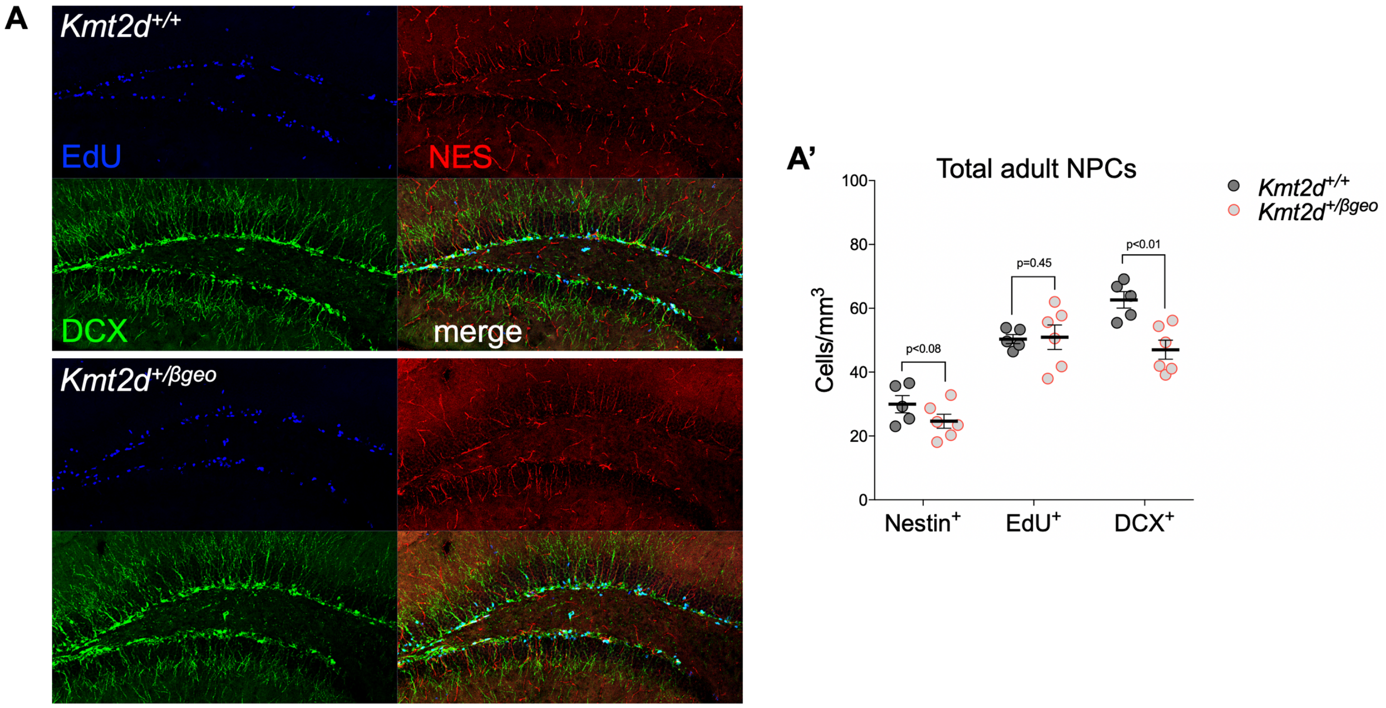

Supplementary Figure 7. Pulse-labeling to birth-date adult-born NPCs *in vivo*. (**A**) Representative immunostaining from *Kmt2d*$^{+/+}$ and *Kmt2d*$^{+/\beta geo}$ mice (5-6 mice per genotype, 10 slices per mouse) of EdU pulse-labeled cells extending a NES^{+} process (NSCs) or DCX^{+} process (NPCs), showing the entire DG area used for quantification. (**A'**) Steady-state quantification of NSCs, NPCs, and EdU-labeled cells for immunostaining quantification in pulse-labeling differentiation experiment, confirming steady-state reduction of adult neurogenesis in *Kmt2d*$^{+/\beta geo}$ mice, despite their increase of pulsed immature neurons (**Figure 5E-E'**). Bars indicate mean ± SEM, Student's t-test (*p<0.05, **p<0.01, ***p<0.001).